TÉCNICO LISBOA

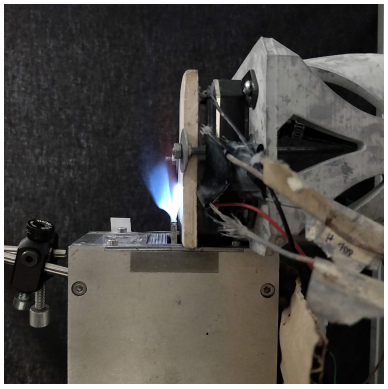

Effect of Different Wall Materials in Thermoelectric Electricity Production

Diogo Manuel Gervásio de Almeida

Thesis to obtain the Master of Science Degree in

Mechanical Engineering

Supervisors: Prof. Edgar Caetano Fernandes
Dr. Sandra Isabel Godinho Dias

Examination Committee

Chairperson: Prof. Carlos Frederico Neves Bettencourt da Silva
Supervisor: Prof. Edgar Caetano Fernandes
Members of the Committee: Prof. Teodoro José Pereira Trindade
Prof. António Cândido Lampreia Pereira Gonçalves

October 2021

"Challenge yourself; it's the only path which leads to growth."

Morgan Freeman

Acknowledgments

This thesis is the culmination of a long challenge and has only became a reality thanks to the support from a large number of people.

First of all, I want to express my deepest gratitude to my family, especially to my mother, my father and my sister, who have always shown their support and motivation for me to succeed.

I am specially thankful to my supervisors for the opportunity and trust placed in me. To Professor Edgar Fernandes, for his dedication and knowledge that contributed to the enrichment of this work. To Dra. Sandra Dias for the experimental supervision and, specially, for the help in reviewing this document.

To my friends and laboratory colleges Bernardo Macara and Diogo Vozone, I am thankful for the support and discussions about experimental work. A special thanks goes to Miguel Santos for sharing the knowledge acquired during his MSc on thermoelectrics.

Finally, I want to thank my ever-lasting friends Francisco Calado, Iva Gonçalves, João Campos, João Coelho, João Silva and Tiago Rua. Their interest in this work and support during the last six years was, undoubtedly, very important for my success. I wish them all the best.

This work was developed at the Thermofluids, Combustion and Energy Systems laboratory of the IN+ - Center for Innovation, Technology and Policy Research.

Resumo

A utilização de barro como material de parede para conversão directa de calor em electricidade utilizando um gerador termoeléctrico (TEG) foi avaliada numa configuração *side wall quenching*. A influência de diferentes misturas de combustível (Metano, Biogás e Biogás + H_2) e as condições de chama na potência e eficiência do TEG foram discutidas. Foi investigada a interacção chama- parede (FWI) de uma chama de pré-mistura em forma de V. A taxa de geração de calor (HRR) e as distâncias de extinção de chama foram analisadas com a quimioluminescência dos radicais OH* e CH*. O campo de velocidade dos gases foi estudado recorrendo a técnicas de *Particle Image Velocimetry* (PIV). Foi utilizada uma parede de aço zincado para comparação de resultados com a parede de barro. Foi desenvolvido um modelo matemático para prever a potência eléctrica gerada para diferentes condições de chama, combustíveis, materiais e espessuras de parede, utilizando o método dos elementos finitos e resultados experimentais obtidos.

Verificou-se que a eficiência e as perdas de energia eléctrica entre materiais aumentam com a temperatura da chama. As distâncias de extinção de chama foram maiores na interacção entre a parede de barro e chama. O fenômeno de extinção de chamas foi governado por perdas de calor para os materiais de parede testados. A convecção mostrou ser mais importante quando se utiliza a parede de barro.

Palavras-chave: gerador termoeléctrico, barro, interação chama-parede, transferência de calor, quimioluminescência da chama

Abstract

The use of clay as the combustor wall material for direct heat-to-electricity conversion using a Thermoelectric generator (TEG) was evaluated in a side-wall configuration burner. The influence of different fuel blends (Methane, Biogas and Biogas + H_2) and flame work conditions in TEG power and efficiency are discussed. Flame-wall interaction (FWI) of a premixed V-shape flame was investigated. Heat release rate (HRR) and quenching distances were analysed with the chemiluminescence of OH* and CH* radicals. The gases velocity field was studied with Particle Image Velocimetry (PIV). A galvanized steel plate was use for comparison with the clay results. A mathematical model was developed to predict electrical power generated for different fuel, flame conditions, wall materials and thicknesses, using the finite element method and experimental results obtained.

It was found that the efficiency and electrical power losses between materials increases with flame temperature. Quenching distances were larger in the flame clay wall interaction. Flame quenching was governed by heat losses for the walls tested. Convection heat losses were more important when using the clay wall.

Keywords: thermoelectric generator, clay, flame-wall interaction, heat transfer, flame chemiluminescence

Contents

List of Tables

List of Figures

List of Publications

This work led to a research article submitted to Applied Thermal Engineering:

- **D. M. G. Almeida***, S. I. G. Dias and E. C. Fernandes. "The impact of Clay as wall material on Thermoelectric power generation and flame-wall interaction."

.

Nomenclature

Acronyms

BG	Biogas.
FWI	Flame-Wall Interaction.
GS	Galvanized Steel.
HOQ	Head On Quenching.
HRR	Heat Release Rate.
HT	Heat Transfer.
HX	Heat Exchanger.
IA	PIV Interrogation Area.
LHV	Low Heating Value.
LPM	Liters Per Minute.
PIV	Particle Image Velometry.
SLPM	Standard Liters Per Minute.
STP	Standard Temperature and Pressure conditions.
SWQ	Side Wall Quenching.
TEG	Thermoelectric Generator.
TE	Thermoelectric.

Chemical species

Al_2O_3	Alumina.
Bi_2Te_3	Bismuth telluride.
CH_4	Methane.
CH*	Excited methylidyne radical.

CO_2	Carbon dioxide.
H_2O	Water.
H_2S	Hydrogen sulphide.
H_2	Hydrogen.
N_2	Nitrogen.
O_2	Oxygen.
OH*	Excited hydroxyl radical.
PbTe	Lead telluride.
SiGe	Silicon-germanium.
TiO_2	Titanium dioxide.
ZrO_2	Zirconium dioxide.

Greek symbols

β	Camera - wall misalignment angle.
χ	Molar fraction.
Δt	PIV time interval between pulses.
δ_{flm}	Flame thickness
$\delta_{q,OH}$	Heat release thickness in the quenching region, derived from OH* chemiluminescence.
η	Efficiency
κ	Thermal conductivity.
λ	Wavelenght of eletromagnetic wave.
μ	Dynamic viscosity.
ν	Kinetic viscosity.
ϕ	Air-fuel mixture equivalence ratio.
ψ	Interpolating function.
ρ	Density.
σ	Electrical conductivity.
τ	Thomson coefficient.

Roman symbols

$\dot{q}$	Heat generation rate.
$\dot{V}$	Volumetric flow rate.
$\overline{\dot{q}'''}$	Average volumetric heat generation rate.
$\mathrm{IA}_{x,y}$	PIV interrogation area width, height.
A	Area.
D	Diameter.
d_q	Quenching Distance.
E	Electrical potencial.
$f/$	Camera aperture f number.
h	Convective heat transfer coefficient.
I	Intensity of image pixel.
I_e	Electrical current.
L	Thermoelectric leg half lenght.
l_s	Burner slit lenght.
M	Image magnification factor.
N	Number of pairs of p and n legs in thermoelectric row.
n	Number of mols.
n_{stoich}	required number of mols of air to oxidate one mol of fuel, in stoichiometric proportions.
Nu	Nusselt number.
o_{IA}	PIV interrogation area overlap.
p	Pressure.
P_{flm}	Flame power.
P_{TEG}	Power generated by TEG.
Pr	Prandtl number.
q	Heat transfer rate.
q''	Heat flux.
R^2	Statistical coefficient of determination.
R_0	Ideal gas constant.

R_e	Electrical resistance.
$R_{e,load}$	Electrical circuit load resistance.
$R_{e,TEG}$	TEG internal electrical resistance.
Re	Reynolds number.
res	Pixel resolution
S	Seebeck coefficient.
T	Temperature.
t	Thickness.
U_m	Voltage measured in acquisition board.
u_r	Relative Uncertainty.
$u_{95\%}$	Uncertainty with a 95% confidence level.
u_σ	Uncertainty standard deviation
U_{cc}	TEG closed circuit voltage.
U_{oc}	TEG open circuit voltage.
V	Velocity
w_s	Burner slit width
x, y, z	Cartesian coordinates.
Y_F	Fuel mass fraction.
$Z\overline{T}$	TEG figure of merit.

Subscripts

brt	Refering to burnt gases.
C, H	Cold and hot sides of TEG.
c, h	cold and hot sides of TEG legs.
$cond$	Conduction heat transfer.
$conv$	Convection heat transfer.
fh	Refering to flame holder dimensions.
flm	Refering to flame.
flm, ad	Refering to adiabatic flame.

$flm, 0$	Point of the flame front closest to the wall.
$flm, 1, 2$	Point in quenching region bounding 25% OH* normalized intensit of the flame.
i, j	Computational indexes.
max, min	Maximum, minimum values.
p, n	p-type and n-type thermoelectric semiconductors.
s	Refering to slit dimensions.
$stoich$	Stoichiometric premixed condition or proportion.
u	Refering to unburnt gases.
$wall$	Refering to the wall surface exposed to flame.
x, y, z	Cartesian coordinates components.
OH	Derived from OH* chemiluminescence information.

Chapter 1

Introduction

1.1 Motivation

In recent decades, the awareness for climate changes has grown. In 2015, the Paris Agreement was signed by 197 countries, representing almost the total greenhouse gas emission worldwide, in a joint effort to limit the temperature rise to under 2 ℃, ideally below 1.5 ℃, above the pre-industrial levels [1].

Energy demands are expected to continue to increase in the next few decades, following the predicted growth in world population and industry. Although the share of renewable sources in electricity production is projected to increase, fossil fuels will still play an important role over the coming years.

At the same time, there is still a vast number of people (almost 1 billion, 13% of world's population [2]) who live in decentralized rural areas, not connected to the grid, that do not have access to electricity. The solution commonly adopted by governments and aid agencies is the construction of mini grids powered by solar photovoltaic panels and batteries, that provide electricity to the village. In this situation, providing a minimum amount of electricity, *e.g.* for lighting, can make a substantial difference.

To power LED lights or charge equipment, thermoelectric generators (TEG) are one of the alternative solutions to solar power in rural electrification. TEG offer great reliability, silent and on-demand electricity source, instantly converting the heat from flames, furnaces or boilers into electricity [3]. The TEG is normally encapsulated between a metallic wall and a heat sink. However, stoves in these locations are usually made of the available materials, namely clay and stone. Clay is a relatively inexpensive material that presents a high potential and versatility, is easy to prepare and set-up which makes it a very useful tool in the move towards establishing environmentally "friendly" technologies [4].

Biomass anaerobic digestion is a biological decomposition process which transforms organic matter, that if disposed without any treatment would be harmful to the environment, *e.g.* soil and water contamination, into biogas (BG) and inorganic substances. The use of biogas helps cutback on fossil fuel usage and reduces greenhouse gas emissions. However, the weak combustion properties of biogas restrict its range of applications. The blending of small amounts of hydrogen (H_2) with biogas enables its direct use in burners without the need for upgrading or purification. The injection of small quantities of H_2 into the gas grid represents an intermediate phase in the growth of hydrogen technology.

1.2 Thermoelectric technology

1.2.1 Theoretical background

Thermoelectric (TE) modules are solid-state (no moving parts), reliable and scalable devices that convert heat directly into electricity, and vice versa. They are made of semiconductor legs, electrical connected, usually in series, with a thin metallic conductor, and fixed to ceramic plates [3].

In any TE device, there are two types of materials, one positively charged and another negatively charged, named p-type and n-type, respectively (Figure 1.1). In the n-type leg, free-electrons carry both charge and heat, while in the p-type leg, this transportation is done by electron-holes. When a temperature gradient is applied to both sides of the device, the charge carriers diffuse from the hot side to the cold side to achieve a new equilibrium state. The concentration of charge carriers increases in the cold side and a positive (negative) potential is built on the cold end of the p-type (n-type) leg [5]. This phenomena is known as the Seebeck effect. When the two legs are joined with the metallic connector, a circuit is formed in which the induced voltage drives the movement of electrons, creating an electrical current.

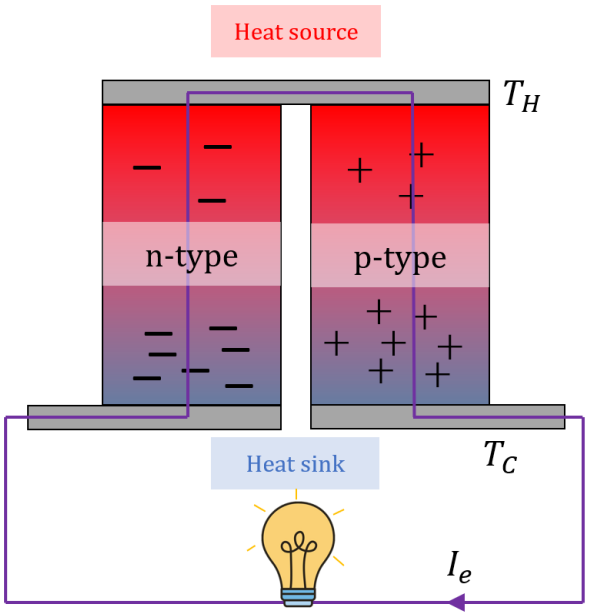

Figure 1.1: A schematic drawing of a thermoelectric device used for power generation applications.

If an electrical current is applied, heat will be generated or absorbed at the junction between the two semiconductors, thus creating a cooling side and a heating side. This phenomena is termed Peltier effect and allows the thermoelectric to be used as a solid-state heating or cooling device, depending on the direction of the applied current [3].

The voltage induced at the thermoelectric terminals is proportional to the difference between the Seebeck coefficient of each leg ($S_p - S_n$), which increases with the thermal gradient in each the leg. To maximize the electricity generated for a given amount of heat supplied to the module, thermoelectric materials have a low thermal conductivity, in order to increase the temperature gradient between the hot

and cold side, and should have high electrical conductivity, to allow the conduction of electricity [6]. The efficiency of the thermoelectric materials is commonly evaluated with the thermoelectric figure of merit $Z\bar{T}$ [5–7], defined as:

$$Z\overline{T} = \frac{(S_p - S_n)^2}{K\, R_e}\overline{T} \tag{1.1}$$

where $K = \kappa L$ is thermal conductance of the parallel equivalent of the two materials and $R_e = L/(\sigma\, A)$ is the average electrical resistance of the n-type and p-type materials, and are evaluate at temperature $\overline{T}$, which corresponds to the average between hot and cold surface temperatures (T_H and T_C, respectively).

From the point of view of a thermodynamic cycle (Figure 1.2a), the efficiency of the TEG, η_{TEG}, can be defined as follows, where q_H is the heat absorbed and P_{TEG} represents the useful work, electrical power generated:

$$\eta_{TEG} = \frac{P_{TEG}}{q_H} \tag{1.2}$$

A load resistance, $R_{e,load}$, is typically connected to the TEG terminals (Figure 1.2b). Results from the numerical model developed by Narjis *et at* [8] show that in order to obtain the maximum power output the ratio between $R_{e,TEG}$ and $R_{e,load}$ must be greater than 1 but less than $\sqrt{1 + Z\overline{T}}$.

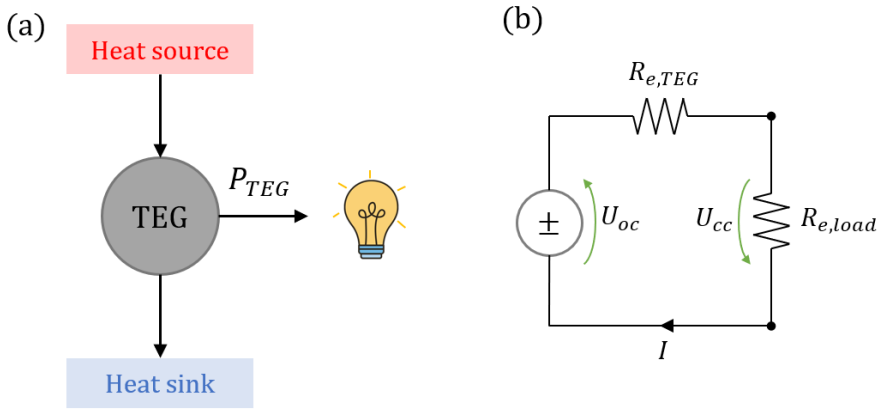

Figure 1.2: A schematic drawing of a thermoelectric (a) thermodynamic and (b) electrical circuits.

In ideal conditions (adiabatic system and matched load resistance, $R_{e,load} = R_{e,TEG}$), η_{TEG} can be described as function of the thermoelectric figure of merit $Z\overline{T}$ and surface temperatures [7]:

$$\eta_{TEG} = \left(1 - \frac{T_C}{T_H}\right) \frac{\sqrt{1 + Z\overline{T}} - 1}{\sqrt{1 + Z\overline{T}} + \dfrac{T_C}{T_H}} \tag{1.3}$$

1.2.2 Applications

The potential use of a thermoelectric to generate electrical power from any heat source has allowed this technology to be used in a vast number of applications [5, 9]. Thermoelectric devices have been widely used to increase the thermal efficiency in the industrial sector [10, 11], specially if the process involves high temperatures and/or high quantities of waste heat.

The scalability and reliability of this devices, and its technological advances, enables its potential use in body-mounted electronic devices such as hearing aids and cardiac pacemakers [12]. The power

requirements of these devices are extremely low, *ca.* 1 mW and 50 μW, respectively.

The largest advances in thermoelectric technology occurred during the space exploration in the 1950s. For missions beyond the orbit of Mars, deep space exploration, the radiant heat flux from the sun is not adequate to power a spacecraft, therefore thermoelectric devices were used to convert the heat generated by nuclear fissile material into electricity [3]. The TEG used were made of Lead telluride (PbTe) and Silicon-germanium (SiGe) and operated in the range of 500 to 900K and 800 to 1300K, respectively

Thermoelectric devices have also been studied as a portable electricity generator unit, as an alternative to batteries and/or solar PV panels, using a small combustion chamber as heat source [13]. Hiranandi *et al* [14] developed a numerical model of a TEG with a micro-combustor. They used two Bismuth telluride (Bi_2Te_3) TEG, suited for temperatures below 450K, and CH_4-Air flames. They achieved a maximum electrical power output of 5.6 W at an efficiency of 6.8% with a $R_{e,load} = 2.8\ \Omega$ load. The maximum power was obtained with a temperature difference of $T_H - T_C \approx 240^\circ C$. Their system had a volume comparable to the one of a conventional electrochemical battery.

Aravind *et al.* [15] developed a micro combustion chamber to pair with two thermoelectric generators and produce electricity. The TEGs were placed between the combustor exterior walls and a cooling jacket with flowing water. They achieved a maximum power output of 4.52W, equivalent to a power density of 0.14 W/cm^3, with a maximum conversion efficiency of 4.66%.

Although, the range of applications for the thermoelectric technology is vast, their low conversion efficiency presents a handicap on their potential uses. Several studies have been conducted on TE material optimization and leg geometries [16]. Erturun *et al.* [17] studied the effect of different thermoelectric leg geometries (rectangular, trapezoidal, cylindrical, and octagonal prisms) on thermo-mechanical and power generation performances of thermoelectric devices using the ANSYS finite-element software. They observed that for a thermal gradient of 100 ℃, cylindrical prism legs obtained the greatest electrical power output and efficiency.

1.3 Biogas

Anaerobic digestion is a biological process, that takes place in an oxygen deficient environment, where organic matter reacts with microbial organisms and breakdown into biogas and inorganic matter, which after appropriate treatment can be used as fertilizer. Biogas composition is affected by the origin of the organic waste (urban waste, agricultural waste or manure) and the configuration of the digestion process. Typically, it contains 50% to 75% of methane (CH_4), 30% to 50% of carbon dioxide (CO_2) and traces of nitrogen (N_2), water (H_2O) and hydrogen sulphide (H_2S). The considerable amount of CO_2 in biogas is responsible for its weak combustion properties (low laminar flame speed, low calorific value and poor flame stability), which constitute an obstacle to its range of applications.

One of the possible solutions to widen the range of applications of biogas is to upgrade it, *i.e.* remove the bulk component of CO_2 and minor components, dry the gas and compress it. Hydrogen can also be blended with the biogas to create H_2 enriched biogas. The addition of small quantities of H_2 have been proven to widen the range of flame stability, increase heat release rates and flame speed [18–21].

1.4 Flame-wall interactions and wall material

As a flame approaches a cold surface, there will be a point from which it can no longer survive. This phenomena is often referred to as flame-wall interaction (FWI) or flame quenching. It occurs because a portion of the heat generated by the flame is being absorbed by the wall, or consumed in radical recombination reactions, and not enough is added to the gas, therefore ignition cannot happen. The incomplete reaction promotes the formation of pollutants in the vicinity of the wall. For small combustion chambers, with a high surface-to-volume ratio, FWI is the dominant factor in the pollutant formation and thermal efficiency [20, 22].

One of the main parameters to describe the flame-wall interaction is the quenching distance d_q, and its definition will depend on the type of burner. If the flame lays between two parallel plates or inside a tube (Figure 1.3a), the d_q is characterized by the minimum distance or minimum diameter, for which ignition can occur. If the flame is only bounded by a single wall, d_q equals the length at which the flame stabilizes from the wall, and the FWI is termed head on quenching (HOQ) if the flame propagates in the normal direction to the wall (Figure 1.3b), or side wall quenching (SWQ) if flame propagates parallel to the wall (Figure 1.3c).

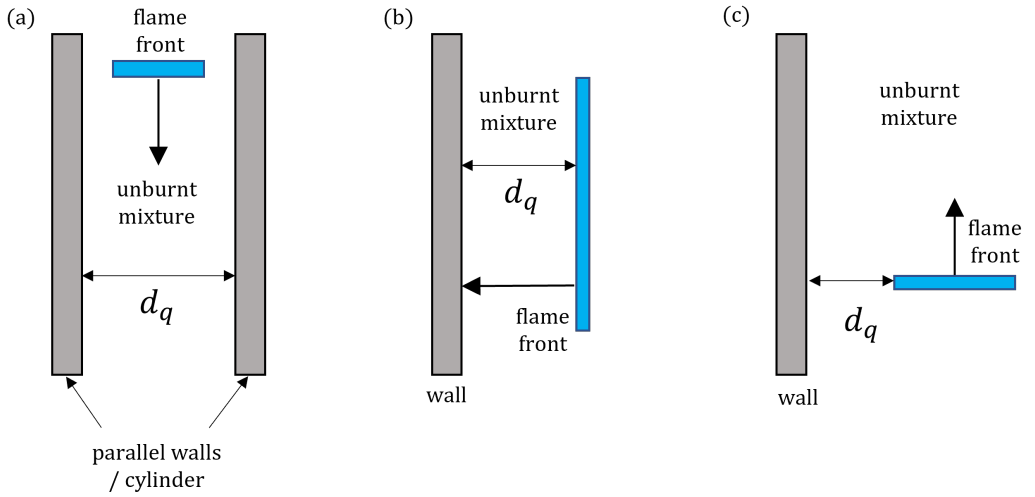

Figure 1.3: Quenching distances measurements for (a) parallel walls or inside a cylinder, (b) head on quenching and (c) side wall quenching.

In literature, flame-wall interaction, in particular side wall quenching, has been a widely discussed topic, which has contributed to a better understanding of the phenomena. Most of authors investigated the influence of flame quenching as a function of wall surface temperature or pressure. However, there are very few studies on the effect of wall material on the quenching distance.

Häber and Stuntz [23] investigated the influence of the equivalence ratio, ϕ (ranging from 0.76 to 13.5), thermal-barrier coatings (Soot, ZrO_2 and TiO_2 on top of ZrO_2) and wall material (steel, cast iron, aluminium) on d_q in a SWQ configuration with two different fuels: CH_4 and propane (C_3H_8). They observed that d_q was the smallest for mixtures with stoichiometric equivalence ratio and decreased with increasing coating thickness. However, for the different materials tested, no significant changes were observed in d_q.

Yang *et al.* [24, 25] evaluated the effect of wall material (zirconia ceramics, stainless steel STS 304 and Si) on flame quenching using two parallel walls and CH_4 stoichiometric premixed flames. They varied the wall temperature from 100 ℃ to 700 ℃ and observed a decrease of d_q with increasing surface temperature T_{wall}, but with different gradients, depending on the wall material. No correlation was found between the wall thermal conductivity and quenching distances. The decrease of d_q with increasing (T_{wall}) was also reported by other studies of flame quenching in SWQ [22, 26] and HOQ [27].

Kim *et al.* [28] also investigated flame wall interaction with different materials and parallel walls. Their work focuses on the influence of thermal and chemical quenching on FWI. They concluded that quenching can be described solely by heat losses at low surface temperatures, between 100 and 350 ℃, but beyond 400 ℃ surface reactions become dominant. At low temperatures, the heat transfer to the wall can be described as pure 1D conduction, based on the Fourier's law [26, 29]:

$$q''_{cond} = -\kappa \frac{dT}{dx} = \bar{\kappa}_u \frac{T_{flm} - T_{wall}}{d_q} \tag{1.4}$$

where $\bar{\kappa}_u$ is the mean thermal conductivity of the unburnt mixture evaluated at $(T_{flm} - T_{wall})$, T_{flm} represents the flame temperature and q''_{cond} corresponds to the heat transferred to the wall by conduction in quenching.

1.5 Scope of the work

The objective of the present work is to evaluate the potential use of clay as wall material for the direct heat-to-electricity power generation using a thermoelectric generator and BG + H_2 lean/stoichiometric flames. Hydrogen is added in small quantities (10% and 20%) to two different biogas mixtures. The influence of wall material on power and efficiency are quantified for different fuels and flame conditions. A galvanized steel wall was used as a reference, to compared the results obtained with the clay wall. A mathematical model capable of predicting the electrical power generated by the TEG using different fuels, flame conditions and, crucially, different wall materials and thicknesses, was also developed.

The effect of wall material in the flame wall interaction was evaluated through the determination of d_q using the chemiluminescence of OH* and CH* radicals to identify the flame front and to estimate the heat release rate in quenching. Additionally, the gases velocity field was studied using Particle image velocimetry techniques (PIV). No research on the flame quenching with a clay wall was found by the time this thesis was written.

Chapter 2

Experimental Setup

2.1 Equipment and setup

The experimental setup (Figure 2.1) can be divided into three major groups: (i) the burning system, which includes the burner and the flow meters used to control gas flow rate; (ii) the TEG system that encompasses the thermoelectric generator itself, the wall, the heat exchanger and water flow meter; and (iii) the data acquisition system which will depend on the type of experiment (power and temperature measurements, chemiluminescence, for analysing quenching distances and heat release rate, or particle image velocimetry).

(a) (b)

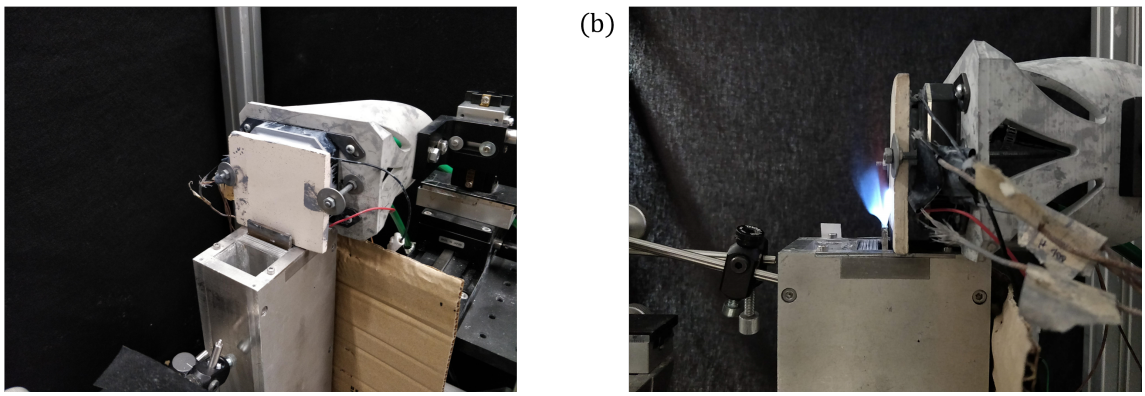

Figure 2.1: Pictures of the experimental setup (a) perspective and (b) side views.

A lamella burner with two slits (length $l_s = 40$ mm and width $w_s = 2$ mm, each) and a stainless steel flame holder (thickness $t_{fh} = 3$mm) were used to acquire a laminar V-shape flame (Figure 2.2). One branch of the flame interacts with a vertical wall, positioned 1.5 mm above the burner and 2 mm away from the flame holder. Connected to the wall is a thermoelectric generator, which extracts heat from the hot wall to produce electricity. An adapted CPU heat exchanger (Phanteks Glacier C350i) is placed on the other side of the TEG to draw the excessive heat out and maintain the temperatures on the cold side of the TEG as low as possible. The TEG used is a commercially available GM200-49-45-30 from European Thermodynamics. The wall is slightly raised above the burner in order to maximized the area for heat transfer, but not enough for the unburnt mixture to escape underneath. This position is

maintained throughout all experiments. The wall is used to protect the TEG from direct contact with the flame and from exceeding the maximum temperature advised by the manufacturer. Information about the TEG module can be found in Table 2.1 and in its datasheet (Appendix A.1).

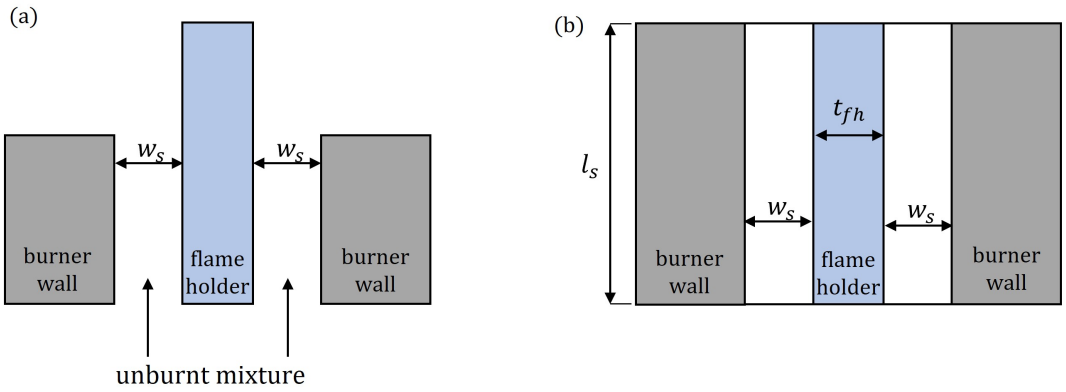

Figure 2.2: Schemes of the burner (a) side and (b) top views.

A galvanized steel (GS) and a clay (cooked at 1250 ℃ for 24 hours) plates, henceforth designated as walls, are used. The walls dimensions and thermal conductivities of the materials are presented in Table 2.2. Chemical composition of both walls and a microscopic image of the clay wall can be found in Appendix C.

Tap water is supplied to the HX and its flow rate is monitored with a Bailey Fischer Porter D10A1197D flow meter (148 l/h capacity). The water enters at the bottom and exits, after passing through a series of fins, at the top of the HX. The wall and the HX are fixed to a 3D printed support. The TEG is hold in place by compression. To reduce thermal contact resistances and improve heat conduction, thermal paste (AG Termopasty HPX, $\kappa = 2.8$ W/mK) is applied to all TEG, wall, and HX surfaces in contact.

Table 2.1: GM200-49-45-30 thermoelectric general characteristics

Dimensions	$62 \times 62 \times 5.8$mm	
Maximum temperature:	$T_{H,max} = 200° C$	$T_{C,max} = 175° C$
Performance for:	$T_H = 200° C$	$T_C = 30° C$
Matched load output power	7.5W	
Matched load resistance	$0.28\Omega \pm 15\%$	
Open circuit voltage	2.8 V	
Heat flow through module	$\approx$ 149W	

Table 2.2: Wall dimensions and thermal conductivity

Material	κ_{wall} [W/mK] [30]	l_{wall} [mm]	h_{wall} [mm]	t_{wall} [mm]
Galvanized steel	56.7	90	75	1.0
Clay	1.3	80	80	6.5

The different fuels blends are obtained by combining CH_4, CO_2 and H_2, drawn from gas bottles (Air liquid Alphagaz 99.95%). Dried compressed air is used to achieve the desired equivalence ratios. Alicat

Scientific M-series mass flow meters were used to controlled each mixture flow rate. The flow meters have a maximum capacity of 5, 5, 1 and 50 SLPM, respectively, and their set points are controlled with an in-house developed program with LabView software. The gases are mixed in a small chamber, which then connects to the burner via a single tube.

2.1.1 Power and temperature acquisition

Six OMEGA k-type thermocouples and a Data Translation DT9828 acquisition board are used to acquired the TEG surfaces and water temperatures. Two thermocouples are placed on each side of the TEG, separated by 30 mm in the y direction (Figure 2.3a). At the inlet and outlet of the HX, a thermocouple is inserted into the water tube, as close as possible to the HX. The acquisition board is connected to a computer, where the readings are monitored, and recorded, using the QuickDAQ software. The bare wires of all thermocouples were coated with varnish to avoid short circuits and false readings. They were tested with boiling water to verify their accuracy *a priori*.

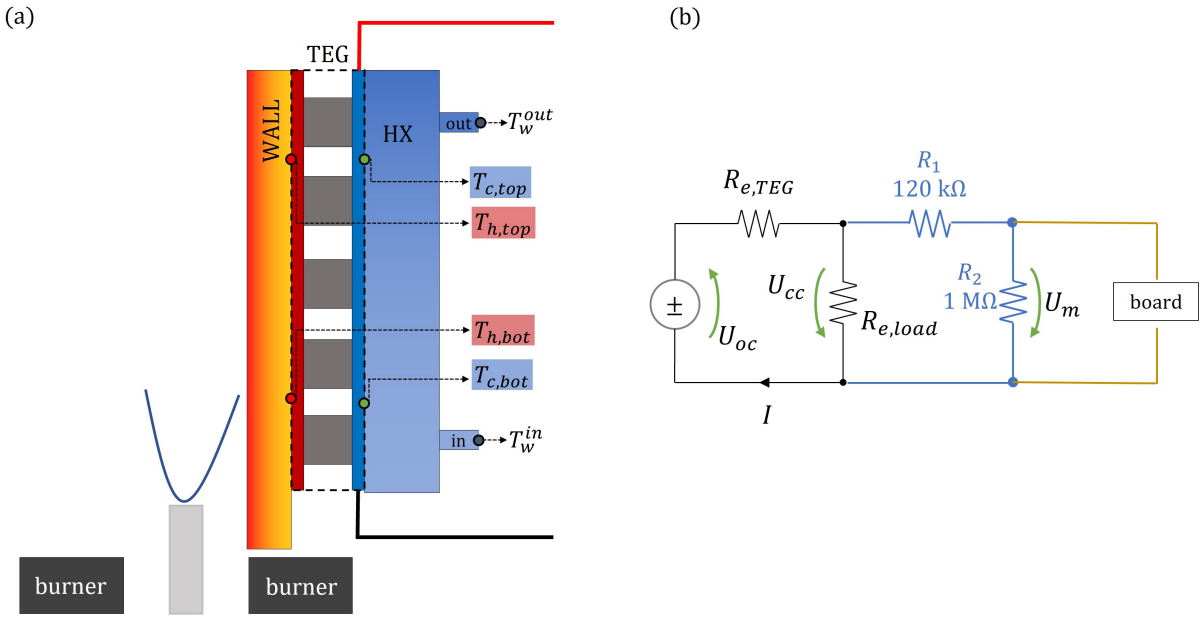

Figure 2.3: Scheme of (a) thermocouple position and (b) electrical circuit.

The TEG terminals are connected to an electrical load, made of ceramic resistances, and a circuit divider, which divides the closed circuit voltage (U_{cc}) by nearly 10 times and enables the monitoring of the voltage U_m with the acquisition board. A scheme of the electrical circuit connected to the TEG terminals is illustrated in Figure 2.3b. The circuit divider is needed because the board can only handle voltages up to 312 mV, but the TEG open circuit voltage (U_{oc}) can reach up to 3V. The load resistance used is $R_{e,load} = 0.281\,\Omega$.

2.1.2 Chemiluminescence

An ANDOR Zyla 5.5 sCMOS camera was combined with a Coastal Optics 105mm f/4.5 UV-Micro-APO lens (permeable to UV light) and a Hamamatsu C9547-03L3 image intensifier to capture the radicals

chemiluminescence (Figure 2.4). The camera has a 5.5 MP sensor and a maximum repetition rate of 50 Hz in single frame acquisition. The image intensifier uses a Multialkali photocathode and has a spectral response from 185 nm to 900 nm and a maximum radiant emittance gain of 6.2×10^3 (for the wavelength of maximum response). The camera was connected to a BNC Model 575 synchronizer, and the two were connected to the computer. The camera configuration and acquisitions were controlled using the Dantec DynamicStudio v5.1 software [31]. The gain on the intensifier was regulated manually with an analogical potentiometer.

Two optical bandpass filters were used to select the emission wavelength of excited radical OH*, with peak emission at 309 nm (Andover 310FS10-50, $\tau_{max} = 17.40\%$, $\bar{\lambda} = 311.142$ nm) and excited radical CH*, with peak emission at 431 nm (Andover 430FS10-50, $\tau_{max} = 50.76\%$, $\bar{\lambda} = 430.850$ nm). These were placed in front of the lens. The chemically excited radicals are from this point forward denoted OH* and CH*.

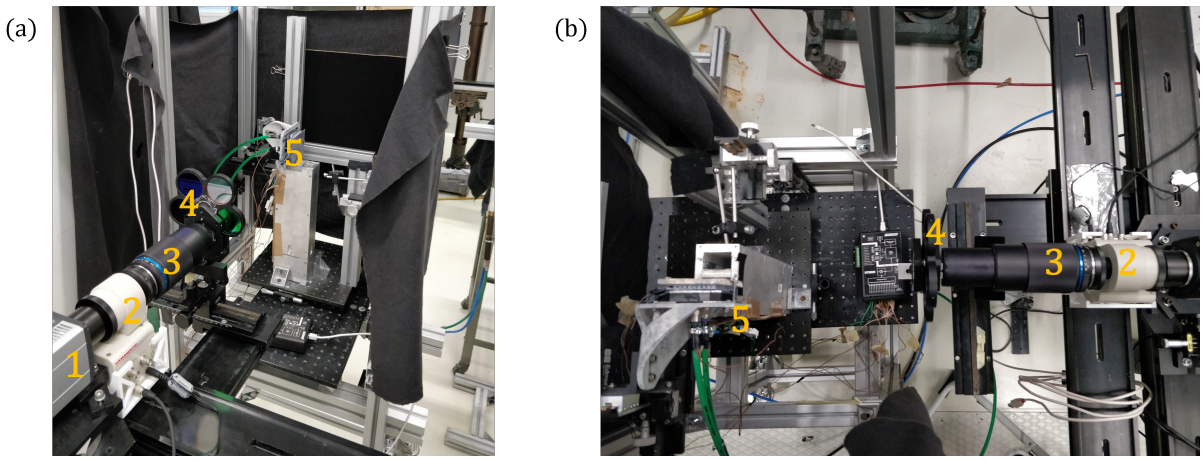

Figure 2.4: Chemiluminescence experimental setup with (1) camera, (2) image intensifier, (3) lens, (4) optical filters, (5) main setup shown in Figure 2.1: (a) perspective and (b) top views.

2.1.3 PIV

Aluminium oxide (Al_2O_3) particles, with diameter $d = 1\mu$m, were used as seeding particles. Their chemical inactivity and high melting point ($T \approx 2350$ K) makes then appropriate for studying combustion reactive flows. The particles were agitated in a flask, with the help of a magnetic stirrer, and carried with the unburnt mixture. The particle density was controlled by regulating the rotational speed of the magnetic stirrer. The optimum density is *c.a.* 10 points per interrogation area.

The Dantec DualPower 65-15 Nd:YAG laser was used to illuminate the Al_2O_3 particles. The laser has two beams, which emit light with a wavelength of 532 nm. After passing through a lens, it produces a light sheet with a thickness of $t_s \approx 1$ mm. The light sheets were adjusted to overlay at the burner exit. Each light pulse lasts for 4ns.

A Nikon 60 mm f/2.8D lens was assembled to the ANDOR camera to capture particle images. The camera operated in double-frame acquisition. The laser and the camera were connected to the synchronizer. Exposure times, number of images, repetition rate and post processing were controlled using the

DynamicStudio software [31].

For acquisitions of the reactive flow (with the flame) a 532 nm CVI Melles Griot light bandpass filter (3nm bandwidth) was placed in front of the lens. The filter is only permeable for the light reflected from the particles, blocking the light emitted by the flame in other wavelengths.

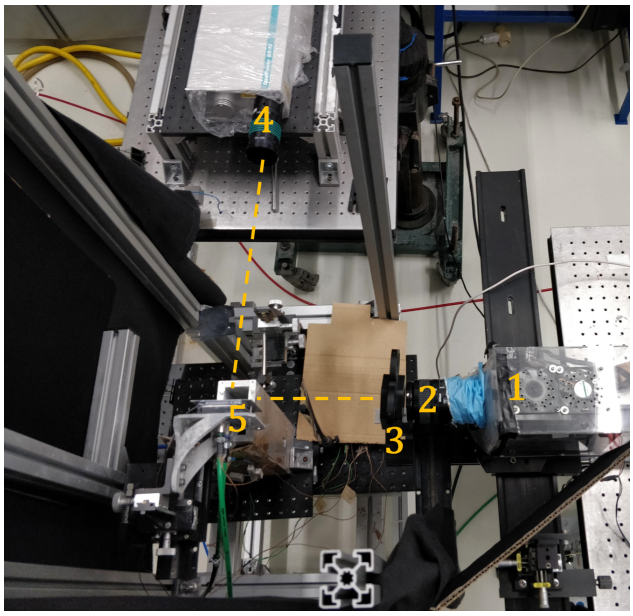

Figure 2.5: PIV experimental setup with (1) camera, (2) lens, (3) 532 nm optical filter, (4) laser and (5) main setup shown in Figure 2.1.

2.2 Experimental procedure

For all analysis, different fuel blends were used: pure methane (BG100) and two blends of biogas (BG80 and BG60). The number after "BG" denotes the amount of CH_4 in the biogas blend (BG80 represents a blend of biogas with 80% CH_4 and 20% CO_2, and BG60 a blend with 60% CH_4 and 40% CO_2). Hydrogen is added to BG60 and BG80 blends in a 10% and 20% volume percentage. The fuel blends are named BG**X** + **Y**% H_2, where **X** is the volumetric percentage of CH_4 in biogas and **Y** is the volumetric percentage of H_2. The molar fraction of each species in the mixture can be calculated from:

$$\chi_{H_2} = \mathbf{Y}/100 \tag{2.1}$$

$$\chi_{CH_4} = \mathbf{X}(1 - \chi_{H_2}) \tag{2.2}$$

$$\chi_{CO_2} = 1 - \chi_{H_2} - \chi_{CH_4} \tag{2.3}$$

The set point for each gas flow meter depends on the burner Reynolds number (Re) and the mixture equivalence ratio. Re was calculated based on the unburnt mixture properties with a characteristic dimension equal to the burner slit width ($w_s = 2$ mm):

$$Re = \frac{V_u \times w_s}{\nu_u} = \frac{[\dot{V}_u/(2 \times w_s \times l_s)] \times w_s}{\nu_u} = \frac{\dot{V}_u}{2 \times \nu_u \times l_s} \tag{2.4}$$

where $\dot{V}_u$ [m^3/s], ρ_u [kg/m^3], μ_u [Ns/m^2] and ν [m^2/s] are the unburnt mixture volumetric flow rate, density, and, dynamic and kinetic viscosity, respectively, and $l_s = 40$ mm is the burner slit length. The Reynolds number studied range from 100 to 350.

Three lean and the stoichiometric equivalence ratios ϕ are used and were calculated from the stoichiometric number of mols of air (n_{air}) required to completely burn one mol of fuel (n_{fuel}), n_{stoich}:

$$\phi = \frac{\mathrm{AFR}_{stoich}}{\mathrm{AFR}} = \frac{[n_{air}/n_{fuel}]_{stoich}}{n_{air}/n_{fuel}} = \frac{n_{stoich}\,\dot{V}_{fuel}}{\chi^{air}_{\mathrm{O}_2}\dot{V}_{air}} \tag{2.5}$$

$$n_{stoich} = 2\chi_{\mathrm{CH}_4} + \frac{\chi_{\mathrm{H}_2}}{2} \tag{2.6}$$

and $\chi^{air}_{\mathrm{O}_2} = 0.21$ is the volumetric fraction of oxygen in the dry air used. All fuel and flame work conditions are summarized in Table 2.3.

Table 2.3: Overview of fuel blends and operating conditions tested.

Reynolds number, Re	100, 150, ..., 300, 350
Equivalence ratio, ϕ	0.7, 0.8, 0.9, 1.0
Base fuels	BG100, BG80, BG60
H_2 dope	0%, 10% ,20%
Min flame power, $P_{flm,min}$	$\approx$ 263 W
Max flame power, $P_{flm,max}$	$\approx$ 1343 W

A room temperature of $T_u = 298.15$ K and atmospheric pressure were assumed at the exit of the burner when computing the volumetric flow rate at standard conditions for temperature and pressure (STP conditions) for the set points of the flow meters, using the ideal gas law $p = \rho_u R_0 T$. The flame power (P_{flm}) was calculated from the mixture low heating value (LHV [J/kg]), ρ_u and fuel mass fraction (Y_F):

$$P_{flm} = \mathrm{LHV} \times \rho_u \times \dot{V}_u \times Y_F \tag{2.7}$$

The Cantera [32] Python module was used to calculate the different mixture properties. The GRI-Mech3.0 mechanism [33] was used to compute transport properties (*e.g.* dynamic viscosity and thermal conductivity), taking into account the transport properties of each species.

The water flow rate was set to 1.23 LPM, which corresponds to 50% of the flow meter's maximum capacity. This flow rate was chosen in order to have comparable results with previous works [34] and was maintained for all analysis.

2.2.1 Power and temperature acquisition

Temperatures at the TEG hot side were closely monitored, specially in mixtures with equivalence ratio close to stoichiometric. When using the GS wall, if any of the temperatures exceeded 195 ℃, the acquisition would be aborted and that work condition is not taken into account. In the case of the clay wall, a more conservative approach was used, the temperatures were limited to 175 ℃. The highest tempera-

ture is expected to be located at the same height of flame extinction, and since clay has a low thermal conductivity and therefore poor heat dissipation, there could be a region of the TEG hot surface with a higher temperature that those measured by the thermocouples.

During initial tests performed with a clay wall, it was observed that the wall would form a crack after *ca.* 3 min with flame, even with weaker mixtures. The heat flux is more intense near the zone where the flame extinguishes, and even more intense with Re close to flashback, which lead to high temperature gradients in the wall and may cause it to crack. Therefore, the lower limit of the Re range was set to one or two intervals higher than the one where flame flashback occurs depending on the equivalence ratio, *e.g.* if flame flashback occurs at $Re = 150$, the Re tested with the clay wall ranged from 200 or 250 to 350. Additionally, the wall was slowly heated with the flame with the lowest T_{flm} (BG60, $\phi = 0.7$) prior to other mixtures, in order to reduce the thermal gradient between the flame and the unheated wall.

The electric power generated, P_{TEG}, is estimated using the Ohm law and the parameters U_{cc} and $R_{e,load}$ using the relation:

$$P_{TEG} = U_{cc} \times I_e = U_{cc} \times \frac{U_{cc}}{R_{e,load}} = \frac{U_{cc}^2}{R_{e,load}} \tag{2.8}$$

This method was also used by other authors to determine P_{TEG} [15].

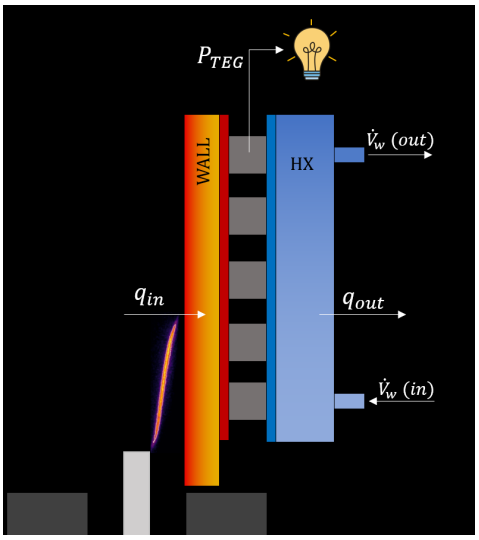

Figure 2.6: Scheme of the system energy balance.

To estimate the heat absorbed from the flame to the TEG, it was considered that the system is adiabatic, the heat absorbed by the TEG is either converted into electricity or rejected to the HX, where all heat is absorbed by the water (Figure 2.6). The total heat flow that enters the device (q_{in}) was estimated from:

$$q_{in} = P_{TEG} + q_{out} = P_{TEG} + \dot{V}_{\mathrm{w}} \times \rho_{\mathrm{w}} \times c_{p_{\mathrm{w}}} \times (T_{\mathrm{w}}^{out} - T_{\mathrm{w}}^{in}) \tag{2.9}$$

where $\dot{V}_{\mathrm{w}}$ [$\mathrm{m^3/s}$] = [LPM] / (1000 × 60), ρ_{w} [$\mathrm{kg/m^3}$] and $c_{p_{\mathrm{w}}}$ [J/kg K] are, respectively, the volumetric flow rate, density and specific heat capacity of water.

The acquisitions lasted 2 min for each condition. A 5 min interval between conditions was adopted to ensure steady state operation of the system.

2.2.2 Flame chemiluminescence

The lens distance to the burner was chosen so that the flame tip could be captured for all the conditions tested and with highest possible resolution. The images acquired had a resolution of 51.26 pix/mm ($res = 19.51\mu$m). A lens aperture of $f/16$ and an exposure time of 10 ms were used. For each flame condition and radical, 30 images were acquired at a rate of 5 Hz in order to obtain a more precise estimation of the quenching distance. The images were captured in a dark environment to reduce background noise

In order to compare images of the same radical between conditions, the gain on the intensifier must be maintained throughout all conditions, that means that for weaker flames, the contrast between the flame and the background will be weaker than for flames closer to stoichiometry. Therefore, to have the best possible contrast for weaker flames, the gain should be near the limit, where the pixels start to saturate, for the flame which has highest chemiluminescence intensity (BG80 + 20% H_2 and BG100, $\phi = 0.9$ and $Re = 200$, for the OH* and CH*, respectively). A 5 min interval between flame conditions was kept so that acquisitions were done when the system was at steady state conditions.

Alignment and wall position

Before the image acquisitions, the wall was carefully align with the camera axis. The determination of d_q is very sensitive to a rotation about the burner's axis. A misalignment angle of 1° can arise to errors in the estimation of d_q of about 350 μm. Therefore, the setup is mounted in a platform capable precise rotational movements.

The method used to align the wall with the camera axis was developed by Häber and Suntz [23] and modified by Santos *et al.* [34], and it uses a stainless steel sphere with diameter $D_{sphere} = 10.3$ mm, fixed to a small rod, that is gently leaded against the wall. From the image acquired (Figure 2.7), the sphere shape was identified using the Hough transform in MATLAB image analysis tools, obtaining the sphere centre coordinates and radius (in pixels). For these images, the smallest lens aperture $f/32$ was used, to acquired silhoutte shapes with sharper edges and facilitate image processing.

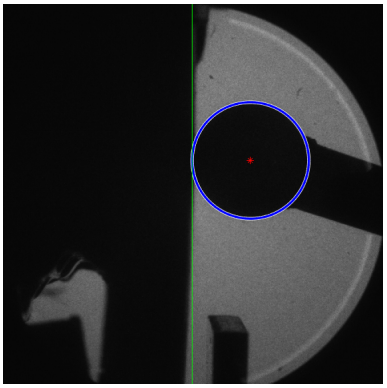

Figure 2.7: Photo of sphere touching the wall at $z = 0$, with the wall aligned.

The alignment process can divided into four steps (Figure 2.8a):

1. With the sphere touching the wall at $z = 0$, the camera position was adjusted until the sphere

center was located close to the half width of the image acquired;

2. The sphere was moved along the z direction in intervals of 2mm, in the positive and negative axis, and images were acquired in each position. The images captured were processed, obtaining the sphere centre coordinates for each position along the z axis and a estimative of the misalignment angle β;
3. Small corrections were made to the platform using the millimetric angle adjuster and the previous step is repeated. If β was less than 0.14 ° (corresponding to a 50 μm error in estimating d_q), we can proceed to the next step;
4. The camera is moved $D_{sphere}/2$ to the right so that the surface is close to the half-width of the image.

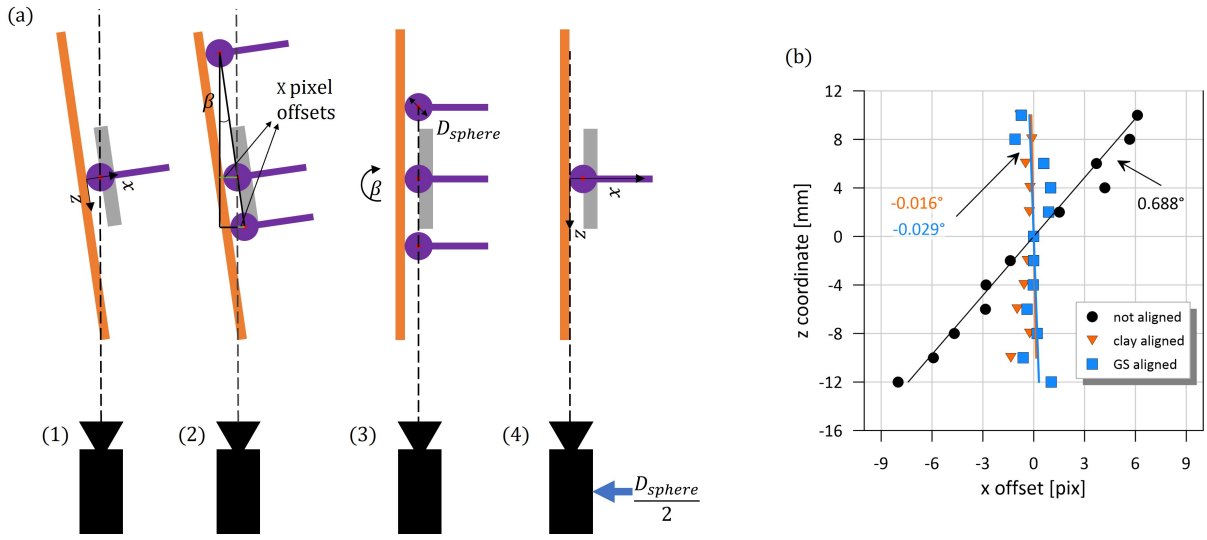

Figure 2.8: Wall alignment (a) steps and (b) initial and final misalignment angles.

In the case of the alignment with the clay wall, the small imperfections at the surface would create errors in the pixel offset and lead to an incorrect alignment. Therefore, a small acrylic was attached to wall, where the sphere would touch it. The angle misalignment was estimated using linear fitting to the data points. The sphere was also used to determined the wall coordinates x_{wall} for measuring the quenching distances. Figure 2.8b presents the final misalignment angle for both walls and an example of the wall not yet aligned.

Image processing

The technique used to identify the flame front depends on the equipment used and on the data with it obtained. The flame front can be tracked using the HRR and its derivative ∇HRR [35–37], the temperature and heat flux profiles in the vicinity of the wall [22, 35, 36, 38], the radicals fluorescence (usually OH) [35, 39, 40] or with the chemiluminescence of flame radicals [23, 34]. In this work, we used the chemiluminescence signal of the radicals CH* and OH* to identify the flame front location.

The flame front region was defined as the zone where the concentration of OH* and CH* radicals is

greater than 50% of its maximum value. Results from Quintino *et al.* [41] show that the concentration of this excited radicals is proportional to their chemiluminescence intensity. This methodology was also implemented by other authors in similar studies [23, 34, 42] to anchor the flame front. The use of 50% intensity rather than the point where chemiluminescence signal vanishes, used by other authors [26, 43], is a more robust technique, since it has better signal-to-noise ratio and is less sensitive to small flame perturbations.

Numerical simulations of 1D adiabatic flame for Biogas + H_2 blends performed by Santos *et al* [34] using the Cantera python module and the GRI-Mech 3.0 mechanism demonstrated that the point where 50% OH* radical concentration correlates well with the midpoint between the maximum HRR and its maximum gradient, whereas the 50% CH* radical concentration correlates better with the location of maximum HHR. Furthermore, the concentration of OH* was shown to have an approximately linear relation with the HRR [44].

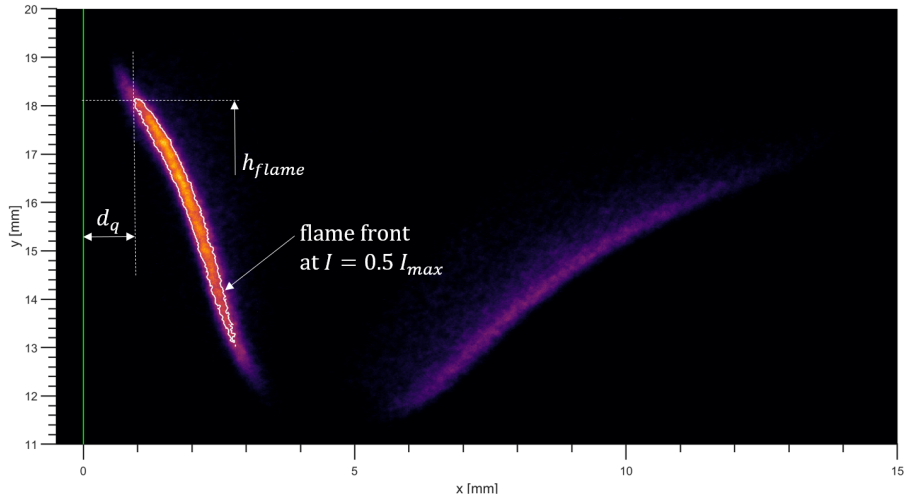

Figure 2.9: Processed image of a photograph for a BG60 flame ($\phi = 0.9$, $Re = 300$) with the flame front position outline in white; the quenching distance d_q is defined as the shortest distance between the wall and the white solid line.

An example of an OH* chemiluminescence image is shown in Figure 2.9. The white solid line highlights the flame front contour, the region of the flame with pixel intensity equal to 50% of its maximum value. To enhance the precision in determining the pixels with 50% intensity, all images acquired were magnified to 5 times their original size, resulting in a resolution close to 3.90 pix/μm. d_q is defined as the shortest distance between the wall and the white solid line:

$$d_q[\mu\text{m}] = (x_{flm,0} - x_{wall})[\text{pix}] \times res[\mu\text{m/pix}] \tag{2.10}$$

where $x_{flm,0}$ and x_{wall} correspond to the most left pixel and wall coordinates.

Given the relation between OH* concentration and HRR, an estimative of the heat released in quenching $\dot{q}'$ can be obtained from the OH* intensity (I_{OH}) along the x axis where it d_q is measured .

$$\dot{q}'_{q,\text{OH}} = \int_{x_{flm,1}}^{x_{flm,2}} I_{\text{OH}} dx \tag{2.11}$$

where $x_{flm,1}$ and $x_{flm,2}$ correspond to left and right pixels with 25% normalized intensity, respectively (Figure 2.10). The distance between the two points defines the heat release thickness:

$$\delta_{q,OH} = x_{flm,2} - x_{flm,1} \tag{2.12}$$

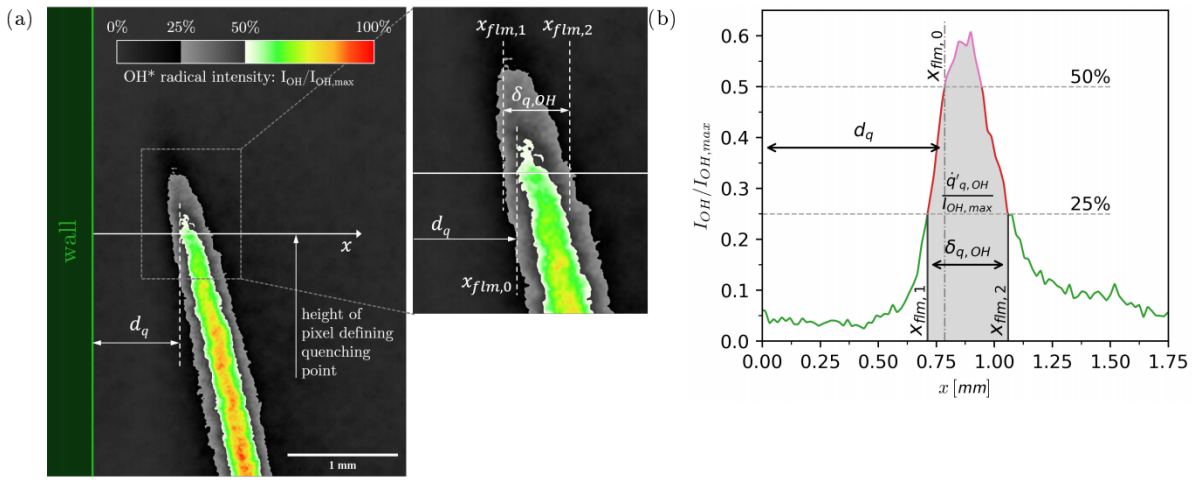

Figure 2.10: Calculation of the heat release thickness $\delta_{q,OH}$ and heat release in quenching $\dot{q}_{q,OH}$ (a) processed image of BG60 + 20% H_2 flame and (b) profile of normalized pixel intensity in the x direction at the height where d_q is measured [34].

2.2.3 PIV

The lens aperture was set to $f/4$, allowing for enough light, reflected from the particles, to enter the camera and the use of small exposure times, which are crucial to avoid the particle motion blur. The camera position was chosen so that the flame holder, the flame and a portion of the flow upstream of combustion could be captured. The images were acquired with a resolution of 32.4 pix/mm (res = 30.86 μm/pix), with a magnification factor M = 4.754. 200 pairs of images were acquired at a rate of 15 Hz, the maximum at double frame acquisition. The laser sheet was aligned with the midpoint of the flame holder ($z = 0$). As for the chemiluminescence images, the acquisitions were made in a dark environment.

The time between the two laser pulses Δt was determined by the flow velocity $[V_x, V_y]$, the image resolution, the size of the chosen interrogation area $[\mathrm{IA}_x, \mathrm{IA}_y]$ and its overlap percentage $[o_{\mathrm{IA},x}, o_{\mathrm{IA},x}]$ through the condition:

$$\Delta t \; < \; min\left(\frac{[\mathrm{IA}_x, \mathrm{IA}_y] \times (1 - [o_{\mathrm{IA},x}, o_{\mathrm{IA},x}]) \times res}{[V_x, V_y]}\right) \tag{2.13}$$

Δt should be lower than the minimum of the two vectorial components. Figure 2.11 illustrates the mentioned parameters.

Since the flow velocity is predominantly vertical, IA_y should be larger than IA_x. The interrogation area was set to $[\mathrm{IA}_x, \mathrm{IA}_y]$ = [16,32], and the overlap to o_{IA} = 75% in both directions. The maximum velocity V_y was based on the experimental results from Santos *et al.* [34]. A time between frames of 75

μs was used. Since the flow is statistically steady an average correlation method was used to process the 200 pairs of images acquired. In this routine, velocity is calculated from a weighted average of all pairs of images and automatically neglects weak correlations, that may result of insufficient particle density in some frames.

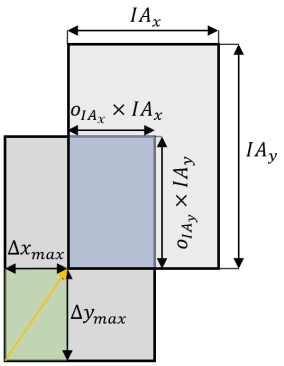

Figure 2.11: Scheme of Interrogation area and overlap.

2.3 Uncertainties

The uncertainty of any variable or result is evaluated with the 95% confidence level and its relative quantity, calculated from:

$$u_r = \frac{u_{95\%}}{a} \times 100 \tag{2.14}$$

where a denotes the average of the population with a $u_{95\%}$ 95% confidence interval. Uncertainties were evaluated following the guidelines from Abernethy *et al.* [45]. For most cases, populations of measurements were assumed normal distributed.

The errors between the actual flow rate passing through a gas flow meter and its set point depend on the flow meter's capacity and the chosen set point. The precision of the air flow meter is equal to $\pm 0.8\%$ of the set point and $\pm 0.2\%$ of the capacity. For the other gases, CH_4 CO_2 and H_2, the errors correspond to the greatest value between $\pm 0.6\%$ of the set point or $\pm 0.1\%$ of the capacity. Precision values correspond to the 99% confidence interval, for a normal distribution that equals to the interval [-$3u_\sigma$, $3u_\sigma$]. The 95% confidence interval can be calculated from the flow meter standard deviation $u_\sigma(\dot{V})$.

Flow meter errors propagate to ϕ, Re and P_{flm}. Considering that $\dot{V}_{fuel} = \dot{V}_{CH_4} + \dot{V}_{CO_2} + \dot{V}_{H_2}$, the variance of the equivalence ratio $u_\sigma(\phi)$ can be calculated from:

$$u_\sigma^2 = \sum_{i=1}^{3} \left\{ \left[\frac{\partial \phi}{\partial \dot{V}_{fuel,i}} \right]^2 \times u_\sigma^2(\dot{V}_{fuel,i}) \right\} + \left[\frac{\partial \phi}{\partial \dot{V}_{air}} \right]^2 \times u_\sigma^2(\dot{V}_{air}) \tag{2.15}$$

where $\dot{V}_{fuel,i}$ corresponds to the volumetric flow rate of each species present in the fuel. The partial derivatives can be computed from Equation 2.5.

The variance of Re can be calculated from:

$$u_\sigma^2(Re) = \left(\frac{1}{2 \times l \times \nu_u}\right)^2 \times \sum_{i=1}^{4} u_\sigma^2(\dot{V}_{u,i}) \tag{2.16}$$

where $\dot{V}_{u,i}$ represents the flow rate of each species in the unburnt mixture.

Finally, the variance of the flame power can be determined from:

$$u_\sigma^2(P_{flm}) = [\rho_{\mathrm{CH_4}} \times \mathrm{LHV}_{\mathrm{CH_4}}]^2 \times u_\sigma^2(\dot{V}_{\mathrm{CH_4}}) + [\rho_{\mathrm{H_2}} \times \mathrm{LHV}_{\mathrm{H_2}}]^2 \times u_\sigma^2(\dot{V}_{\mathrm{H_2}}) \tag{2.17}$$

The 95% confidence interval, and its relative error, was computed from each variable standard deviation, for every flame condition tested. Their average and maximum values are presented in Table 2.4.

Table 2.4: Uncertainties of gases and water flow rates, equivalence ratio, Reynolds number and flame power; average and maximum errors calculated based on all conditions tested.

		$u_{95\%}$		u_r	
		avg	max	avg	max
$\dot{V}_{air}$	[SLPM]	0.150	0.188	1.01%	1.69%
$\dot{V}_{\mathrm{CH_4}}$	[SLPM]	5.3×10^{-3}	8.9×10^{-3}	0.42%	0.83%
$\dot{V}_{\mathrm{CO_2}}$	[SLPM]	3.6×10^{-3}	5.6×10^{-3}	0.79%	3.09%
$\dot{V}_{\mathrm{H_2}}$	[SLPM]	1.3×10^{-3}	3.2×10^{-3}	0.43%	1.07%
Re		2.185	2.698	0.90%	1.47%
ϕ		0.009	0.016	1.07%	1.79%
P_{flm}	[W]	3.125	5.228	0.40%	0.74%
$\dot{V}_w$	[LPM]	0.049	0.049	3.97%	3.97%

2.3.1 Power and temperature acquisition

The acquisition board where the temperatures and the voltage U_m were measured has a 95% confidence interval $u_{95\%} = \pm 0.18$ ° C when measuring the temperatures (based on the datasheet information) and a bias error of $u_b(U_m) = \pm 20\mu V$ and a precision of $\pm 0.03\%$ when measuring U_m.

The uncertainty of the closed circuit voltage U_{cc} can be derived from the linear relation between U_m and $U_{cc}(U_{cc} = g\,U_m,\ g = 1120/120)$, and the standard deviation of U_{cc} during the 2 min acquisitions, denoted $u_\sigma^2(U_{cc,TEG})$:

$$u_{95\%}(U_{cc}) = \sqrt{u_b^2(U_{cc}) + k^2[u_\sigma^2(U_{cc}) + u_\sigma^2(U_{cc,TEG})]} \tag{2.18}$$

where $k = 2$ to obtain the 95% confidence interval. The variance $u_\sigma^2(U_{cc})$ and bias $u_b(U_{cc})$ of the closed circuit measurements

$$u_\sigma^2(U_{cc}) = [g \times u_\sigma(U_m)]^2 \tag{2.19}$$

$$u_b(U_{cc}) = g \times u_b(U_m) \tag{2.20}$$

The uncertainty of the P_{TEG}, derived from Equation 2.8, can be calculated from:

$$u_\sigma^2(P_{TEG}) = \left[\frac{\partial P_{TEG}}{\partial U_{cc}} \times \sqrt{u_\sigma^2(U_{cc}) + u_\sigma^2(U_{cc,TEG})}\right]^2 \tag{2.21}$$

$$u_b(P_{TEG}) = \frac{\partial P_{TEG}}{\partial U_{cc}} u_b(U_{cc}) = \frac{2U_{cc}}{R_{e,load}} u_b(U_{cc}) \tag{2.22}$$

$$u_{95\%}(P_{TEG}) = \sqrt{u_b^2(P_{TEG}) + k^2 u_\sigma^2(P_{TEG})} \tag{2.23}$$

The uncertainties of each variable were calculated for all conditions tested. Their average and maximum values are presented in Table 2.5

Table 2.5: Uncertainties of the closed circuit voltage, power yield and temperature; minimum, average and maximum uncertainties calculated for all conditions tested.

		$u_{95\%}$		u_r	
		avg	max	avg	max
U_{cc}	[V]	32.5 $\times 10^{-3}$	42.7 $\times 10^{-3}$	3.87%	4.72%
P_{TEG}	[W]	0.042	0.095	1.52%	2.60%
Temperature	[° C]	-	0.18	-	0.09%

2.3.2 Flame chemiluminescence

The uncertainty in the determination of the quenching distances depends on systematics errors caused by the pixel resolution and the lens optical aberrations, and statistical errors related with the uncertainty in the determination of the wall position x_{wall} and different evaluated flame tip positions, induced by small perturbations in the flow. Since the flame quenching occurs near the half-width of the image, it can be assumed that in that region distortions, and thus optical aberrations, are insignificant and can be neglected. The uncertainty associated with the determination of x_{wall} was quantified by repeatedly leaning the sphere against the wall, acquiring 20 independent values of x_{wall}.

The quenching distance uncertainty can be described as:

$$u_{95\%}(d_q) = \sqrt{u_b^2(res) + k^2[u_\sigma^2(flmfront) + u_\sigma^2(x_{wall})]} \tag{2.24}$$

where $u_b(res) = 19.51\mu m/2$ is the systematic error caused by pixel resolution and, $u_\sigma(flmfront)$ and $u_\sigma(x_{wall})$ correspond to the standard deviation in the determination of flame front and wall position, respectively. For the 95% confidence interval, $k = 2$.

Table 2.6: Uncertainties in the determination of the quenching distances; entries without a value for u_r do not have a reference value.

		$u_{95\%}$		u_r	
		avg	max	avg	max
determine x_{wall}	μm	-	26.63	-	-
flame front position	μm	82.9	177.2	6.85%	12.92%
quenching distance d_q	μm	87.8	179.3	7.28%	13.33%

2.3.3 PIV

The uncertainty of the flow field was estimated with peak height ratio methodology [46]. Radial uncertainty limits based on a 95% confidence interval were determined for all interrogation areas. Table 2.7 presents the average and maximum uncertainty and its relative value, for two different fuels tested.

Table 2.7: Radial uncertainty bounds for two fuels tested with $\phi = 0.7$ and $Re = 300$

		$u_{95\%}$		u_r	
	fuel	avg	max	avg	max
Clay	BG60	0.044	0.124	1.68%	4.14%
	BG100	0.039	0.124	1.29%	4.13%
GS	BG60	0.036	0.124	1.38%	4.14%
	BG100	0.038	0.124	1.27%	4.14%

Chapter 3

Mathematical Model

The mathematical model developed in this work aims to predict the power generated for a given wall material and wall thickness, with different fuels and flame conditions. To do so, the model requires information about the fuel composition (BG composition and H_2 concentration), flame condition (equivalence ratio and burner Reynolds number), electrical load resistance and the wall characteristics (thermal conductivity and wall thickness).

The model can also be adapted to predict the work conditions for which a given power output is achieved. Other parameters can also be studied, *e.g.* the influence of the water or air flow rate through the heat exchanger on the electricity production with the TEG.

Given that the heat transferred from the flame to the wall is not constant along the vertical axis, and in order to have a more precise and robust description of the heat transfer, a two-dimensional model was developed. It uses the finite element method to solve the heat transfer differential equation in two dimensions.

Some simplifications and assumptions were made during the development of the model:

1. The system can be reduced to two dimensions, homogenous along width;
2. Negligible thermal and electrical contact resistance between all parts;
3. Negligible thermal and electrical losses in the electrical connectors between p and n legs, since they have high thermal and electrical conductivities, and small thickness;
4. Isotropic properties of all materials;
5. No heat losses to the surroundings.

3.1 Finite Element Method

The two-dimensional heat transfer problem can be described by a second order differential equation with a single dependent variable, the temperature T, over the domain Ω with a boundary Γ [47]:

$$-\nabla.(\kappa\,\nabla T) = f(x,y)\,\text{in}\,\Omega \tag{3.1}$$

The terms on the left side of the equation correspond to heat conduction and the terms on the right the heat generation. Following the steps described in [47], the weak form (or weighted integral statement) over a typical element Ω_e, which will be the basis of the finite element model of Equation 3.1 , was developed:

$$\int_{\Omega_e} \left(\kappa \frac{\partial w}{\partial x} \frac{\partial T}{\partial x} \; + \; \kappa \frac{\partial w}{\partial y} \frac{\partial T}{\partial y} \; - \; w \, f \right) dx \, dy - \oint_{\Gamma_e} w \; [\hat{q}_n - h \, (T - T_\infty)] \; ds \; = \; 0 \tag{3.2}$$

where w is a weight function, h [W/m^2K] is the convective heat transfer coefficient and T_∞ is the temperature of the surrounding fluid medium.

The finite element model of the Equation 3.2 was obtained approximating T to the temperature of the element T^e, which is equal to the sum of all nodal values multiple by the interpolating function ψ^e of the corresponding node, and replacing w by ψ^e, obtaining a system of equations that describe the heat conduction problem in an element:

$$[K^e + H^e] \, \{T^e\} = \{f^e\} + \{P^e\} + \{Q^e\} \tag{3.3}$$

where

$$K^e_{ij} = \int_{\Omega_e} \left(\kappa \frac{\partial \psi^e_i}{\partial x} \frac{\partial \psi^e_i}{\partial x} + \kappa \frac{\partial \psi^e_i}{\partial y} \frac{\partial \psi^e_i}{\partial y} \right) dx \, dy \tag{3.4}$$

$$F^e_i = \int_{\Omega_e} f \psi^e_i \, dx \, dy \; + \; \oint_{\Gamma_e} \hat{q}^e_n \psi^e_i \, ds \; \equiv \; f^e_i \; + \; Q^e_i \tag{3.5}$$

$$H^e_{ij} = h^e \oint_{\Gamma_e} \psi^e_i \psi^e_j ds, \quad P^e_i = h^e \oint_{\Gamma_e} \psi^e_i T_\infty ds \tag{3.6}$$

After creating the matrices and vectors in Equation 3.3 for all elements of the domain, these were assembled into a single matrix or vector using the correspondence between global and element nodes.

Once the global matrix and vectors have been established, and empty lines or columns (all zeros) removed, the system of equations can be solved,

$$\left[K^G + H^G\right] \left\{T^G\right\} = \left\{F^G\right\} + \left\{P^G\right\} \Leftrightarrow \left\{T^G\right\} = \left[K^G + H^G\right]^{-1} \left\{F^G \; + \; P^G\right\} \tag{3.7}$$

The domain Ω was discretized using linear rectangular elements (Figure 3.1). Their interpolation functions are written as [47]:

$$\psi^e_1 = \left(1 - \frac{\bar{x}}{a}\right) \left(1 - \frac{\bar{y}}{b}\right), \quad \psi^e_2 = \frac{\bar{x}}{a} \left(1 - \frac{\bar{y}}{b}\right), \quad \psi^e_3 = \frac{\bar{x}}{a} \frac{\bar{y}}{b}, \quad \psi^e_4 = \left(1 - \frac{\bar{x}}{a}\right) \frac{\bar{y}}{b} \tag{3.8}$$

The temperature derivatives of each element can be calculated from:

$$T^e = \sum_{i=1}^{n} T^e_i \psi^e_i, \quad \frac{\partial T^e}{\partial x} = \sum_{i=1}^{n} T^e_i \frac{\partial \psi^e_i}{\partial x}, \quad \frac{\partial T^e}{\partial y} = \sum_{i=1}^{n} T^e_i \frac{\partial \psi^e_i}{\partial y} \tag{3.9}$$

The heat flux vector $\vec{q}$ of each element can be obtained from the temperature derivatives

$$\vec{q} = -\kappa \nabla T = -\kappa \frac{\partial T^e}{\partial x}\vec{x} - \kappa \frac{\partial T^e}{\partial y}\vec{y} \tag{3.10}$$

One node can be connected to up to four elements, therefore the nodal heat flux components are obtained by averaging the values of the surrounding elements. The difference between the multiple values will decrease with the refinement of the mesh [47].

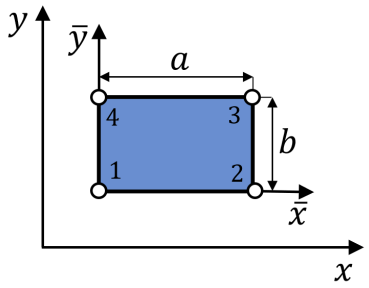

Figure 3.1: Linear quadratic element.

3.2 TEG governing equations

The conversion of heat into electricity with a TEG incorporates different thermoelectric effects in both n and p legs and in the metallic connectors.

The heat conduction through each leg, with section area A_{leg} (A_{leg} = 20.25 mm^2 for the TEG used in this work), can be written as:

$$q = A_{leg}\, \kappa\, \nabla T \tag{3.11}$$

where κ is the thermal conductivity of the material. When a thermal gradient is applied to the TE legs, the flow of electrons or holes from the hot to the cold side causes the build up of an electromotive force proportional to the Seebeck coefficient (S[V/K])(Seebeck effect):

$$E = -S \nabla T \tag{3.12}$$

The electromotive force then drives the electrons from one leg to the other, through the metallic connectors. When the current I_e flows through the junctions with a discontinuity in Seebeck coefficient, heat $\dot{q}$ is generated or absorbed (Peltier effect):

$$\dot{q} = I_e\, \Delta\, T \tag{3.13}$$

The Peltier effect is the counterpart of the Seebeck and it is what allows TE to generate (heater) or absorb (cooler) heat. Within the legs, if the current flows in the same/opposite direction of the heat, then, by the Thomson effect, heat is being generated/absorbed in the TE legs:

$$\dot{q} = \tau\, I_e\, \nabla T \tag{3.14}$$

where $\tau = T \times dS/dT$ is the Thomson coefficient. Finally, as in every electrical circuit, when the electrical current flows through the TE legs with electrical conductivity σ, heat is generated (Joule effect):

$$\dot{q} = \frac{2L}{A_{leg}\,\sigma}\,I_e^2 \tag{3.15}$$

The energy balance of the aforementioned effects can be written as:

$$\begin{cases} \dfrac{d}{dx}\left(\kappa_p \dfrac{dT_p}{dx}\right) + \dfrac{d}{dy}\left(\kappa_p \dfrac{dT_p}{dy}\right) - \dfrac{\tau_p\, I_e}{A_{leg}}\left(\dfrac{dT_p}{dx}\right) + \dfrac{I_e^2}{A_{leg}^2\,\sigma} = 0 \\ \dfrac{d}{dx}\left(\kappa_n \dfrac{dT_n}{dx}\right) + \dfrac{d}{dy}\left(\kappa_n \dfrac{dT_n}{dy}\right) + \dfrac{\tau_n\, I_e}{A_{leg}}\left(\dfrac{dT_n}{dx}\right) + \dfrac{I_e^2}{A_{leg}^2\,\sigma} = 0 \end{cases} . \tag{3.16}$$

where the terms of the equation correspond to, transport of heat by conduction in the x and y direction, Thomson effect and Joule heating, respectively. The constants κ, τ and σ, as well as Seebeck coefficients are evaluated at temperature T_p and T_n for the p-type and n-type leg, and their equations can be found in the TEG datasheet (Appendix A.1).

Since the heat generated/absorbed due to the Peltier effect occurs at the metallic connectors, their contributions are accounted at the leg ends. For a pair of legs, the heat generated/absorbed at its ends can be calculated from:

$$\begin{cases} q''_{Peltier,x=-L} = \dfrac{-I(S_p^{T_h} - S_n^{T_h})\,T_h}{2\,A_{leg}} \\ q''_{Peltier,x=L} = \dfrac{I(S_p^{T_c} - S_n^{T_c})\,T_c}{2\,A_{leg}} \end{cases} \tag{3.17}$$

where the superscript T denotes the temperature at which S is evaluated and L is the half length of the leg ($L = 1.9$ mm for the TEG used). T_h and T_c represent the temperatures at the hot side and cold side of the legs, right after/before the ceramic plates (Figure 3.2).

The TEG legs are electrically connected in series (Figure 3.2) and arranged in a matrix structure. Each row i contains N_i pair os legs. For the TEG module used in this work, each row contains 5 pairs of legs, except the top and bottom rows which have one leg less. The voltage built up at the TEG terminals, U_{oc}, can be calculated from:

$$U_{oc} = \sum_{i=1}^{10} N_i \int_{T_c}^{T_h} [S_p(T_p) - S_n(T_n)]\,dT \tag{3.18}$$

The TEG internal electrical resistance, $R_{e,TEG}$ was calculated from the leg materials electrical properties and the aluminium cables (diameter $d_{cable} = 0.6$ mm, length $L_{cable} = 11$ mm) welded to the TEG terminals.

$$R_{e,TEG} = \sum_{i=1}^{10} N_i \int_{-L}^{L} \left[\frac{1}{A_{leg}\,\sigma_n^{Tp}} + \frac{1}{A_{leg}\,\sigma_n^{Tn}}\right] dx \; + 2 \times \frac{L_{cable}}{A_{cable}\,\sigma_{Al}} \tag{3.19}$$

From the voltage induced at the TEG terminals and the resistances, the current I_e can be calculated:

$$I_e = \frac{U_{oc}}{R_{e,TEG} + R_{e,load}} \tag{3.20}$$

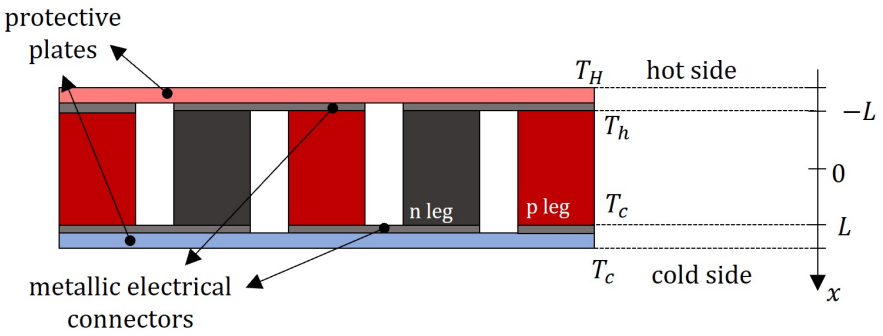

Figure 3.2: Schematic view of one row of the TEG.

The electrical power generated, P_{TEG} can finally be calculated from its electrical analog

$$P_{TEG} = I_e^2 \, R_{e,load} \tag{3.21}$$

Since the thermodynamic circuit was evaluated in two dimensions and the electrical circuit symplified to one dimension, the difference between heat flows q_H and q_C is not equal to P_{TEG}.

The thermoelectric properties (κ, σ and S) and the heat generation/absorption terms require information about the temperature distribution along the leg to be computed. Therefore, an iterative routine was implemented to solve the system. On the first iteration, it is assumed a constant value for k along the TEG legs and the thermoelectric effects are not considered. In the following iterations, the thermoelectric properties are calculated with the temperature distribution of the previous iteration. If the relative difference of I_e and $R_{e,TEG}$ between successive iterations was smaller than 10^{-4}, the iterative process stops and the model returns the desired outputs.

3.3 Boundary Conditions

Since the Equation 3.1 is a second order differential equation, it requires two boundary conditions. The model can either work with two essential or two natural boundary conditions (BCs).

3.3.1 Essential boundary conditions

The TEG surface temperatures, T_H and T_C, were used to solve the system of equations and to estimate the thermal conductivity of the ceramic protective plates of the TEG. The temperatures $T_H = 200$℃ and $T_C = 30$℃ were used as boundary conditions and the thermal conductivity was modified until P_{TEG} equals the value from the TEG datasheet. The final result was a thermal conductivity equal to $\kappa = 3.675$ [W/mK].

In order to solve the system of equations 3.7 with surface temperatures as boundary conditions, for an imposed temperature at the node j, the value of $K^G(i,j) \times T_j$ was subtracted to the line i of the vector F^G

$$F_i^G = F_i^G \; - \; K^G(i,j) \times T_j \tag{3.22}$$

To validate the model for other conditions, the power generated was calculated with the TEG with $R_{e,load} = R_{e,TEG}$ and different combinations of temperatures T_H and T_C as boundary conditions. The obtained results were compared with the values in the datasheet, an average difference of 0.03 W was observed. This overlap between the model and the datasheet can be observed in Figure 3.3a. The temperature distribution and streamlines across the TEG with $T_H = 200$ ℃ and $T_C = 30$ ℃ are illustrated in Figure 3.3b. The streamlines are obtained from the heat flux vectors (Equation 3.10).

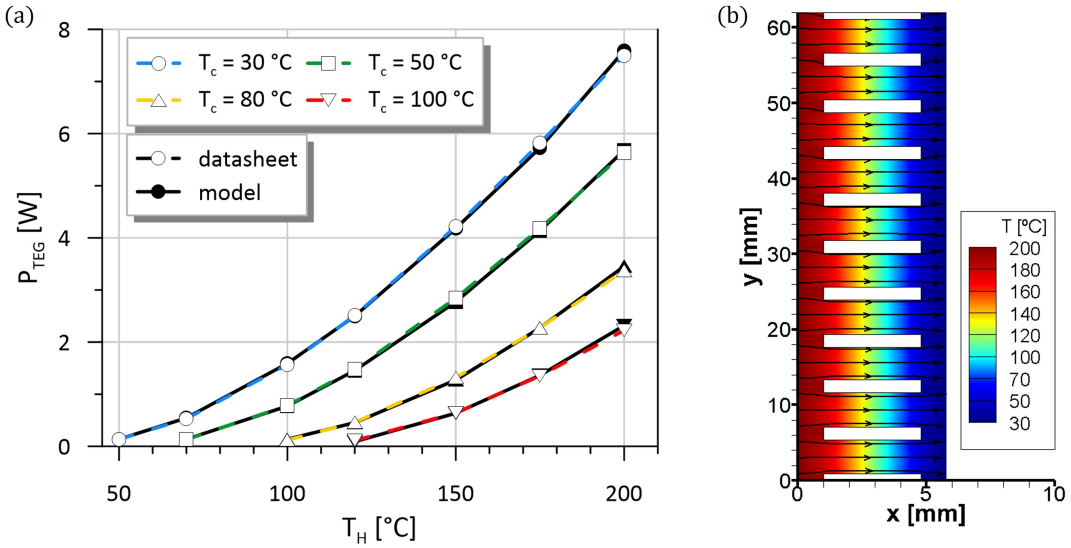

Figure 3.3: (a) Variation of P_{TEG} with T_H and T_C surface temperatures; dashed lines with unfilled markers denote the reference values from the TEG datasheet whilst solid black lines with filled markers the results obtained with the mathematical model (b) temperature distribution and streamlines across the TEG with $T_H = 200$ ℃ and $T_C = 30$ ℃.

3.3.2 Natural boundary conditions

The heat flux from the flame and burnt gases to the wall is characterized by peak heat flux in the region of flame quenching, transported by conduction, followed by convective heat transfer of the hot gases. Heat flux profiles obtained by two research groups are presented in Figure 3.4. Kosaka *et al.* [22] estimated heat fluxes using the Fourier's law (Equation 1.4) and the temperature gradient close to the wall, measured using Coherent anti-Stokes Raman spectroscopy (CARS). Results from Zirwes *et al.* [42] were obtained with CFD simulations. As the authors suggested, their results correlate well with the experimental ones if multiple by a factor of 1/1.8.

Westbrook *et al.* [37] suggested that a CH_4 + Air premixed flame in quenching extinguishes as the flame temperature approaches $T_{flm} \approx 1500$K. The fraction of the total heat that is transferred in quenching can, thus, be estimated from d_q, the TEG temperatures and q_{in}:

$$\frac{q_q}{q_{in}} = \frac{\kappa_u / d_q (T_{flm} - T_H) \times l_s \times \delta_{flm}}{q_{in}} \tag{3.23}$$

Given that this fraction is close to 1%, the conduction contributions can be neglected.

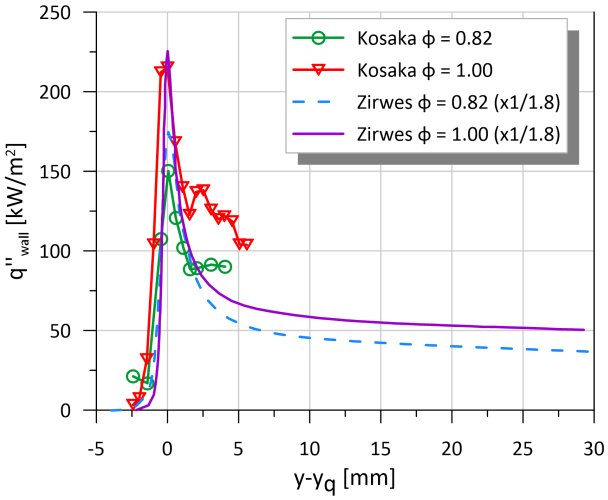

Figure 3.4: Wall heat flux q''_{wall} for BG100 flames in SWQ; y_q corresponds y coordinate where quenching occurs.

The convective heat flux between burnt gases and the wall can be calculated from:

$$q''_{conv}(y') = h_{y'}\,(T_{brt} - T_{wall}) \tag{3.24}$$

where $h_{y'}$ represents the convective heat transfer coefficient at a distance y' from the leading edge ($y' = 0$). T_{brt} and T_{wall} denote the temperatures of the burnt gases and at the wall surface. Given the magnitude of velocities of the flow and the small area where heat transfer occurs, the temperature of the burnt gases can be assumed to be equal to the adiabatic flame temperature $T_{flm,ad}$.

The Nusselt number Nu can be written as a function of h_y or described as a function of the Reynolds and Prandtl number Pr:

$$Nu = \frac{h_{y'}\,y'}{\kappa} = a\,Re_{y'}^{1-b}Pr^{1/3} \tag{3.25}$$

That correspond to a hydrodynamic boundary layer described as:

$$\delta = c\,y'\,Re_{y'}^{-b} \tag{3.26}$$

where δ corresponds to the height of the boundary layer.

Although there is not a reference velocity to correctly define the boundary layer, it is possible to describe the development of a hypotetical boundary layer by tracing isolines with a specific V. Figure 3.5a presents the velocity contours and isolines for a BG100 flame with $Re = 300$ and $\phi = 0.7$ interacting with the GS wall. The points of the isoline with $V = 1.9$m/s (Figure 3.5b) with $23\,mm < y < 38\,mm$ ($y' = y - 23$) were adjusted to the Equation 3.26 to obtain the value of the constant b. A value of $b = 0.667$ and $b = 0.652$ were obtained with an uncertainty of $u_\sigma < 0.006$ for the GS and the clay wall. Different flame conditions may cause small variations in the value of b, but since its influence on the overall heat flux is very small, a constant value of b was assumed for all conditions.

The constant a of Equation 3.25 was estimated by minimizing the mean squared error between the experimentally obtained P_{TEG} and the results calculated with the model. To reduce computational time,

the error function was minimized for results of BG80 flames, instead of the results from the different fuel blends. To obtain the area for heat transfer, results from OH* chemiluminescence with the GS wall were used to obtain the flame height.

The gas properties (κ, Pr and υ) were evaluated at the average between flame and wall temperatures $T = (T_{flm,ad} + T_{wall})/2$. The fluid properties were the result of a 1D freely propagating flame simulation using the Cantera [32] Python module, with GRI-Mech3.0 [33] mechanism to compute the transport properties.

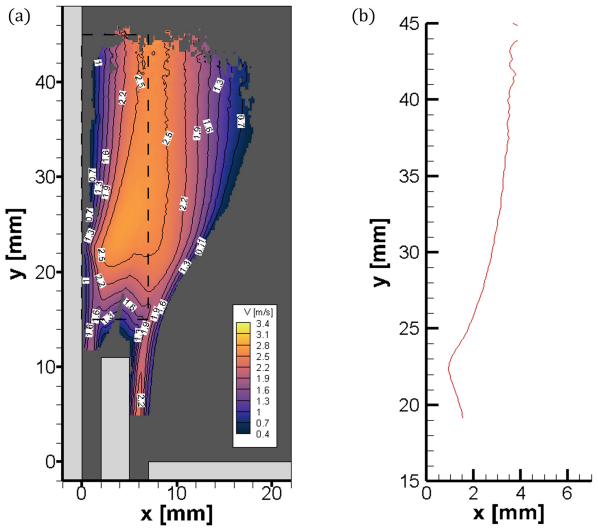

Figure 3.5: (a) Velocity magnitude for BG100 flame with $\phi = 0.7$ and $Re = 300$ interacting with the GS wall and (b) isoline where $V = 1.9$m/s.

Chapter 4

Results

In this chapter, an analysis of the results obtained experimentally and from the mathematical model is performed. It begins with a characterization of the TEG operation with the clay wall where the influence of flame conditions and fuel blends is discussed, followed by the analysis with the GS wall and the influence of wall material. The values and tendencies predicted by the model are compared with the experimental ones. Then, the effect of wall material on flame wall interaction is studied, first through the analysis of quenching distances and the heat release rate, followed by a investigation of the velocity field.

4.1 TEG Performance analysis

To evaluate the performance of the TEG, tests were realized for all fuel blends, Re and ϕ (Table 2.3). As equivalence ratios approach stoichiometry, the increase in the flame speed led to resonating flames at higher Re (Re = 300 and Re = 350). On the other hand, for certain fuels, for lower Reynolds (Re = 100 and Re = 150) flame flashback occurred. In the setup used (flame in SWQ), the flame flashback is characterized by the flame branch further away from the wall (Figure 2.1b) to burn upside down, *i.e.* from the base of the burner up to the flame holder. Conditions where flame flashback occurred were not evaluated.

4.1.1 Clay wall

For a fixed Re, P_{TEG} increased significantly with the increase of ϕ. On the other hand, increasing Re had a negligible effect on P_{TEG}, for a fixed ϕ. The temperature difference between both sides of the TEG (T_H - T_C) also increased with ϕ. Higher ΔT yields larger voltage drops at the TEG terminals (Seebeck effect), which results in the increase of P_{TEG}. An example of the influence of work conditions is presented in Figure 4.1(a) for BG80 flames, P_{TEG} is represented by solid lines with different colours and markers, depending on the equivalence ratio. Power and efficiency maps for the other fuel blends can be seen in Appendix B.1.

The thermoelectric efficiency η_{TEG} was estimated from the total heat that enters the module q_{in} and

the electrical power generated P_{TEG}:

$$\eta_{TEG} = \frac{P_{TEG}}{q_{in}} \tag{4.1}$$

The flame conditions had the same impact on η_{TEG} as for P_{TEG} and ranged from 1.80% to 2.76% for all fuels and flame conditions. The minimum was observed for BG60 with $Re = 150$ and $\phi = 0.7$ and the maximum for BG80 with $Re = 300$ and $\phi = 1.0$.

Since T_C fluctuates at most $5° C$ between work conditions, the fluctuations of P_{TEG} and η_{TEG} (from Eq. 1.3) will depend almost entirely of the oscillations of T_H. For this reason, the maximum power and TEG efficiency, in each fuel blend, were attained for the highest ϕ tested.

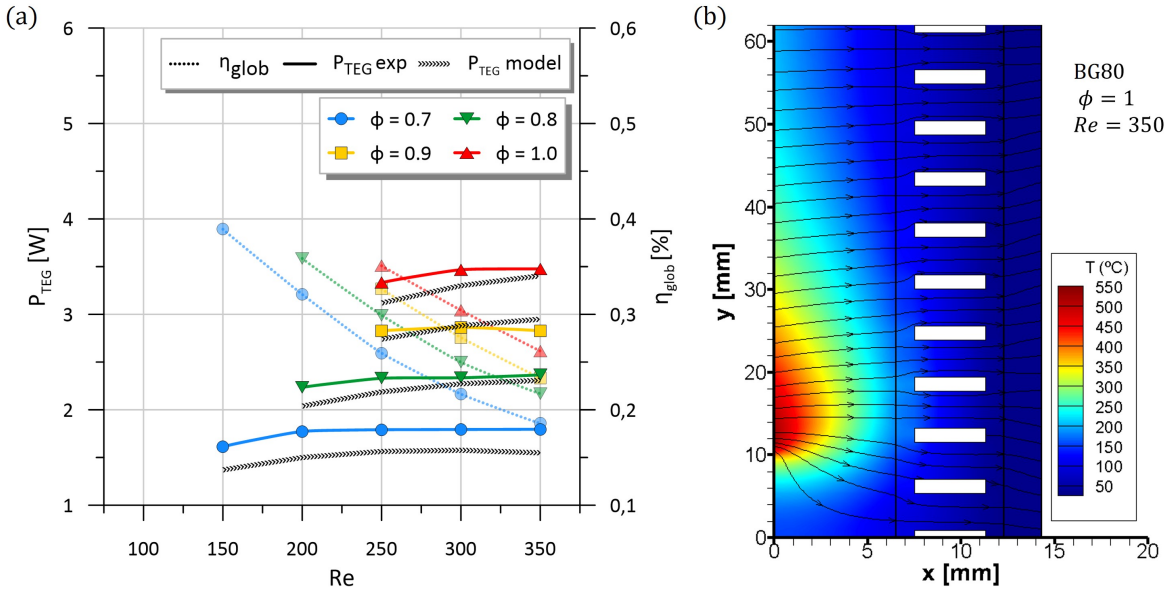

Figure 4.1: (a) Map of P_{TEG} and η_{glob} for BG80 flames with the clay wall; continuous lines link experimental P_{TEG} whilst dotted lines correspond to η_{glob}; black lines denote the values obtained with the mathematical model (b) temperature distribution and streamlines for BG80 with $\phi = 1$ and $Re = 350$.

The global system efficiency was estimated from the flame power P_{flm} and P_{TEG}:

$$\eta_{glob} = \frac{P_{TEG}}{P_{flm}} \tag{4.2}$$

For a fixed ϕ, η_{glob} decreases rapidly with the increase of Re, as shown in Figure 4.1(a) by the dotted lines, with different colours and markers depending on ϕ, for BG80. For all fuels and conditions η_{glob} ranged from 0.17% to 0.39%. Since η_{HT} is almost insensitive to changes in the Reynolds, the system efficiency losses with increasing Re must relate with the heat transfer efficiency η_{HT}:

$$\eta_{HT} = \frac{q_{in}}{P_{flm}} \tag{4.3}$$

For the work conditions studied, η_{HT} ranged from 8.66% to 19.69%, the lowest values attained for high Re. For BG80, the lowest η_{HT} was 8.93%, obtained for $\phi = 0.7$ and $Re = 350$ while the highest was 19.69%, obtained for $\phi = 0.7$ and $Re = 200$. For a fixed Re, small gains in η_{HT} were observed when increasing ϕ, which may be attributed to the small increase of the n and p-type legs thermal conductivity.

Since the fluctuations of η_{HT} are larger than the ones of η_{TEG}, the heat transfer efficiency is the dominant factor in the system's efficiency. The tendencies of P_{TEG} and efficiencies with the work conditions were observed for all fuel blends tested.

The estimations of P_{TEG} obtained with the mathematical model developed in this work (chapter 3) are presented in Figure 4.1a through the black lines. The values predicted by the model were very similar to the experimental results, with an average difference of 0.18 W for all fuels and flame conditions. The low thermal conductivity of clay causes the heat to flow essentially in the x direction as is illustrated by the streamlines in Figure 4.1b. This is then reflected on the temperature distribution upstream of flame quenching (at *ca.* $y = 10.5$ mm for BG80, $\phi = 1$ and $Re = 350$), which are significantly lower than the temperatures downstream ($y < 10mm$).

Diluting BG100 (CH_4) with CO_2, in a 80/20 and 60/40 proportion, had a similar impact on P_{TEG} and η_{glob} as the reduction of equivalence ratio. In both cases, the decrease of combustible fuel causes the loss of flame and burnt gas temperatures, and lower heat release rate, which generates lower TEG surface temperatures. Adding 20% of CO_2 to BG100 causes an average power reduction of 0.11 W ($\pm$0.026 W, 1σ-standard deviation). Adding other 20% to what is now BG80 causes power losses in the range of 0.17 W $< \Delta P_{TEG} <$ 0.67 W. The largest differences occur at stoichiometric equivalence ratios. Blending H_2 to the BG mixtures mitigates the electrical power losses caused by CO_2 dilution.

The power losses and gains between fuels tend to increase as ϕ approaches stoichiometric. The power increments to BG60 with different enrichment techniques are given in Table 4.1 for the equivalence ratios tested.

Table 4.1: Average and standard deviations of the P_{TEG} [W] gains with different enrichment techniques relative to BG60 and the clay wall.

ϕ	10% H_2	20% H_2	50% CH_4
0.7	0.16 ± 0.01	0.21 ± 0.01	0.25 ± 0.01
0.8	0.09 ± 0.03	0.14 ± 0.03	0.21 ± 0.03
0.9	0.16 ± 0.01	0.62 ± 0.12	0.32 ± 0.04
1.0	0.28 ± 0.01		0.63 ± 0.05

From this analysis, one can see that, for lower equivalence ratios ($\phi = 0.7$ and $\phi = 0.8$), blending CH_4 in a 50/50 proportion with BG60 (acquiring BG80) is better than adding H_2 in a 20/80 proportion. On the other hand, for $\phi = 0.9$, the gains with 20% H_2 blending are bigger.

4.1.2 Influence of wall material

The equivalence ratio has the same impact on P_{TEG} with the GS wall as previously described with the clay wall. However, the increase of Re resulted in small increments of P_{TEG}, becoming less pronounced for $\phi = 0.7$ and high Reynolds numbers. The trends observed with the GS wall, in regard to flame work conditions, are in accordance with the results from Santos *et al.* [34] with an aluminium wall. The influence of flame conditions on P_{TEG} and η_{glob} with the GS wall are illustrated in Figure 4.2(a) for BG80 flames. The P_{TEG} fluctuations due to flame conditions were also reflected by the mathematical model

(black lines in Figure 4.2(a)). The values of P_{TEG} obtained with the mathematical model deviated, on average, 0.10 W from the value measured experimentally.

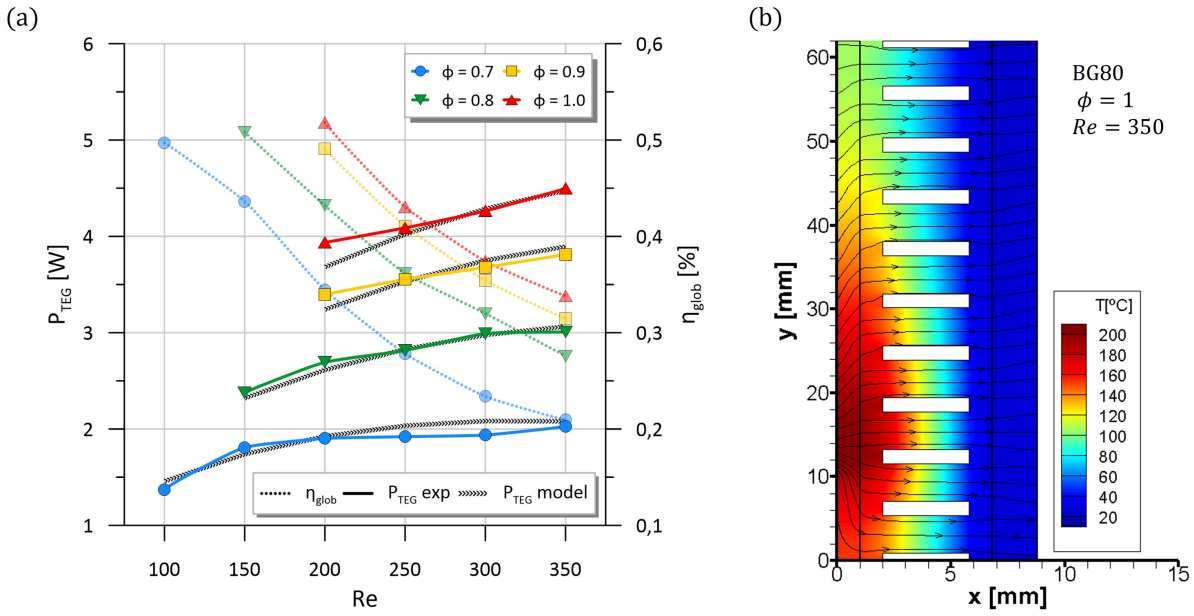

Figure 4.2: (a) Map of P_{TEG} and η_{glob} for BG80 flames with the GS wall; continuous lines link experimental P_{TEG} whilst dotted lines correspond to η_{glob}; black lines denote the values obtained with the mathematical model (b) temperature distribution and streamlines for BG80 with $\phi = 1$ and $Re = 350$.

The high κ_{wall} of the GS wall ($\kappa_{wall} = 56.7$ [W/mK]) allows the intense heat flux from flame quenching to dissipate downstream, as illustrated through the streamlines of the heat flux obtained with the mathematical model (Figure 4.2b). Overall, the power generated with the GS wall is higher than the achieved with the clay wall, with the same fuel and work conditions. The difference in P_{TEG} between GS and clay, ΔP_{TEG}, increased with equivalence ratio and Re. For $\phi = 0.7$, ΔP_{TEG} is the smallest, *ca.* 0.2 W. The maximum ΔP_{TEG} was 1.02 W, observed for BG80 with $\phi = 1.0$ and $Re = 350$. The higher κ_{wall} and smaller thickness of the GS wall, compared to the clay wall, lead to an increase of the heat transfer efficiency, $0.69\% < \Delta\eta_{HT} < 4.27\%$. Higher temperatures on the TEG hot surface resulted in higher thermoelectric efficiency, with $\Delta\eta_{TEG}$ up to 0.31%, and global efficiency, with improvements up to $\Delta\eta_{glob}$ 0.09% ($\Delta\eta_i = \eta_i(GS) - \eta_i(clay)$).

With respect to the influence of fuel blends in the electrical power output with the GS wall, the same trends were observed, adding CO_2 causes a reduction of P_{TEG} which are compensated when H_2 is blended. Table 4.2 presents the power gains for the different enrichment techniques. From this analysis, it can be seen that blending 50% of BG100 with BG60 is the method which results in more power gains. Larger standard deviations arise from the greater sensitivity of the system to small flame perturbations and to Re.

Compared to the GS wall, the clay wall has a much lower thermal conductivity and larger thickness, and therefore a higher thermal resistance, which should make a good thermal insulator and achieve lower temperatures on the hot surface of the TEG. However, the temperatures obtained for both walls with the lowest thermocouple (positioned at $y = 16$ mm from the bottom of the TEG) were very similar, always

smaller than 15 ℃. With the increase of ϕ, temperatures in the top part of the TEG (obtained with the thermocouple positioned at $y = 16$ mm from the top of the TEG), where heat transfer is dominated by convection, exhibit a larger difference, up to 30 ℃.

Table 4.2: Average and u_σ of the power gains with different enrichment techniques relative to BG60 and the GS wall.

ϕ	10% H_2	20% H_2	50% CH_4
0.7	0.31 ± 0.17	0.32 ± 0.13	0.24 ± 0.08
0.8	0.29 ± 0.13	0.23 ± 0.06	0.38 ± 0.10
0.9	0.29 ± 0.06	0.25 ± 0.05	0.42 ± 0.03
1.0	0.12 ± 0.07	0.49 ± 0.09	0.63 ± 0.13

The small κ_{wall}(clay) makes heat flow through the wall almost unidirectional (Figure 4.1b), with negligible vertical heat dissipation, which means that the largest differences (compared to GS) in temperature should occur upstream of the quenching zone. This hypothesis was verified by analysing the temperature profiles at the hot side of the TEG obtained from the model with both walls (Figure 4.3). The power losses between the two materials may be attributed to this difference.

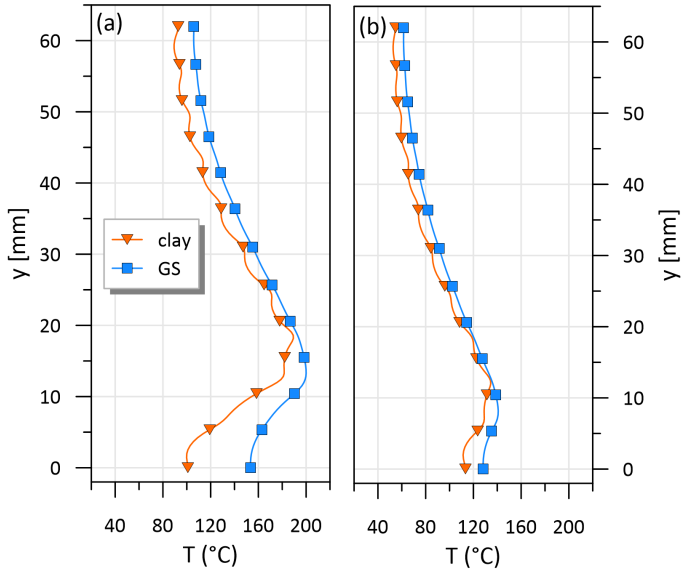

Figure 4.3: Temperature profiles for BG80 with (a) $\phi = 1.0$ and $Re = 350$, and (b) $\phi = 0.7$ and $Re = 150$.

To better understand the contribution of wall material, flame conditions and fuel blend to the power generated, we attempted to relate P_{TEG} with the wall's thermal conductivity (κ_{wall} [W/mk]) and thickness (t_{wall} [m]), Reynolds number and adiabatic flame temperature ($T_{flm,ad}$ [K]), which varies almost linearly with ϕ from 0.7 to 0.9 for BG100 flames [48] and encompasses the effects of adding CO_2 and H_2, with the equation:

$$P_{TEG} = k\, r_{wall}^{a}\, T_{flm}^{b}\, Re^{c} \tag{4.4}$$

where $r_{wall} = t_{wall}/\kappa_{wall}$ represents the thermal resistance per unit area. In addition to the results obtained in this work, values of P_{TEG} obtained with an aluminium wall ($90 \times 75 \times 1$ mm) presented by

[34] were also incorporated. The parameters a, b, c and k were determined by finding the minimum the mean squared error of the error function:

$$F(k,\, a,\, b,\, c) = \left| P_{TEG} - k\, r_{wall}^{a}\, T_{flm}^{b}\, Re^{c} \right| \tag{4.5}$$

The final correlation is presented in Figure 4.4. The equation obtained shows good agreement with the experimental values for all materials, fuels and flame work conditions. The obtained exponents indicate that:

- T_{flm} is the dominant factor on P_{TEG} and, since b = 3.79 > 1, for successive increments of T_{flm}, the gains on power yielded will increase;
- since c = 0.342 < 1, the gains of P_{TEG} obtained by increasing Re will decrease, until a point where the effects of Re are no longer noticed;
- since a = -0.0363 <0, for a fixed wall thickness and successive increments of κ_{wall}, the gains on power generated will decrease.

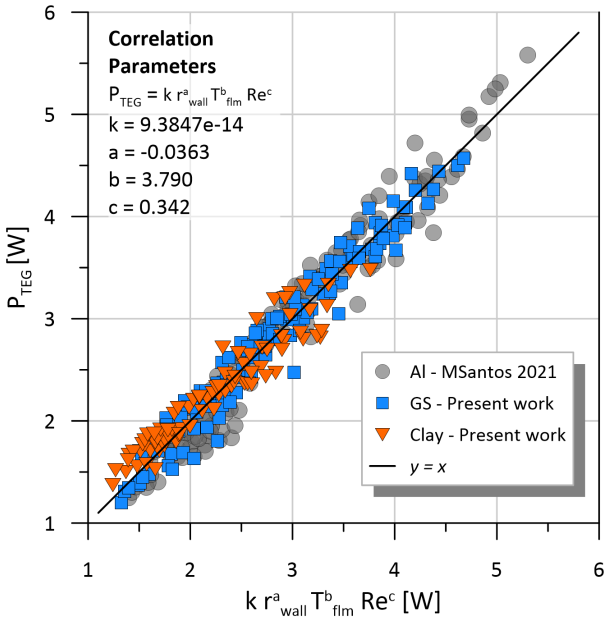

Figure 4.4: Correlation of P_{TEG} using an equation of the type $P_{TEG} = k r_{wall}^{a} T_{flm}^{b} Re^{c}$.

.

4.2 Quenching distances and HRR

Quenching distances were measured for all fuels blends with different flame work conditions. With the clay wall two different Reynolds numbers and two equivalence ratios were selected, Re = 200 and Re = 300, and $\phi = 0.7$ and $\phi = 0.8$. For the GS wall, all equivalence ratios and the same two Reynolds were chosen, excluding those where temperatures on the TEG hot side exceeded 200 ℃.

For the two walls studied, quenching distances increased with the blending of CO_2 (Figure 4.5) and decreased with H_2 enrichment (Figure 4.5) and with the increase of equivalence ratio.

Flames with higher Re stabilize further away from the wall (larger d_q).For flames with $\phi = 0.7$ interacting with the clay wall, the ratio $d_q(Re = 300)/d_q(Re = 200)$ was approximately constant, on average 1.129 (with a u_σ of only 0.018) and 1.162 ($u_\sigma = 0.045$) using the OH* and the CH* chemiluminescence respectively. With the GS wall, and considering all equivalence ratios and fuel blends, $d_q(Re = 300)/d_q(Re = 200) = 1.167$ with a standard deviation of 0.0914 using the OH* chemiluminescence and 1.172 ($u_\sigma = 0.064$) using the CH*.

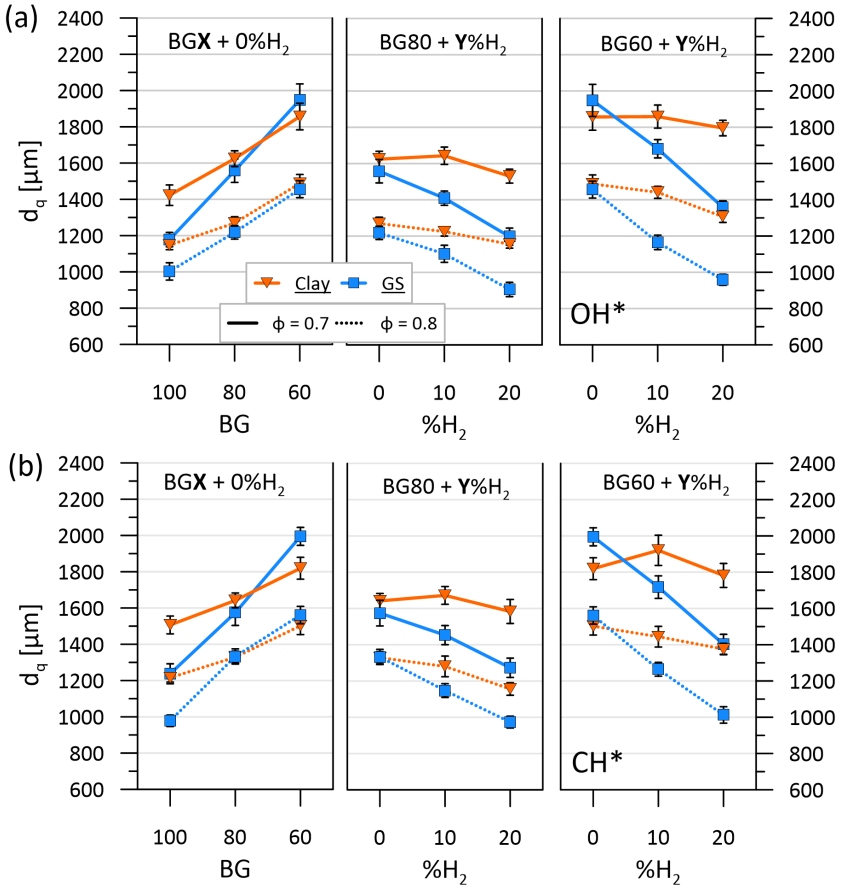

Figure 4.5: Quenching distances for all fuel blends tested, $\phi = [0.7, 0.8]$ and $Re = 300$, determined from (a) OH* and (b) CH* chemiluminescence; error bars represent the u_σ of the 30 different d_q values calculated.

For most of the conditions studied, the value of d_q obtained with the CH* chemiluminescence was bigger than with the OH* by an average of 42 μm (average of all fuels, flame conditions and walls). This is in accordance with the numerical simulations perform by Santos *et al.* [34], who reported a difference of 84 μm between the peaks of CH* and OH* concentration.

With the exception of BG60 and $\phi = 0.7$, quenching distances measured for the clay wall are larger than for the GS wall. With the addition of H_2 to the biogas blends (BG80 and BG60), the d_q difference between clay and GS walls tends to increase.

Kosaka *et al* [22] observed a decreased of 50 μm in the quenching distances of stoichiometric CH_4 flames when increasing the wall temperature from 330K to 450K. Due to small thickness and good

thermal conductivity of the GS plate, the temperature difference between the two sides of the wall is very small and can be assumed $T_{wall} \approx T_H$. This is not valid for the clay wall, hence T_{wall} was estimated by calculating the heat flux, in the quenching zone, with the Fourier law (Equation 1.4) and T_H. For the conditions tested, temperatures at the TEG hot surface varied at most 40K between the conditions tested, a small difference compared to $T_{flm} - T_{wall}$, which is in the order of 1100K for GS and 800K for clay. The variation of wall temperature with fuel and flame conditions is, therefore, expected to have a small impact on the fluctuations of quenching distance between fuels.

Flame quenching is dominated by heat losses to the wall, at lower wall temperatures, as mentioned in the introduction (chapter 1), and that d_q decreases with increasing surface temperature. Habër *et al.* [23] considered that for surface temperatures under $T_{wall} < 500K$, quenching can be described solely by heat losses, for lean and stoichiometric premixed CH_4 flames. For H_2 flames, reactions may occur at lower surface temperatures since the radicals which recombine are the ones that take part in the crucial exothermic, low activation energy reactions which then trigger other reactions. The reduction of important radicals in the flame forces it to stabilize at a higher distance from the wall. For CH_4 + Air [49] or H_2+O_2 [38] premixed flames, one of the most important recombinations reactions at the wall is:

$$H + OH + M \rightarrow H_2O + M \tag{4.6}$$

Since the concentration of H and OH species increases when H_2 is blended, and given the difference in the surface temperatures between materials, this may explain the small variation of d_q with increasing content of H_2 with the clay wall, comparatively to the GS wall (Figure 4.5).

Following the William's second criterion for flame extinction [50], if the flame front is modelled as a slab near the wall with thickness δ_{flm} (Figure 4.6), the heat losses to the surroundings must approximately balance the rate at which heat is being generated by chemical reactions inside the slab ($d_q \times \delta_{flm} \times l$).

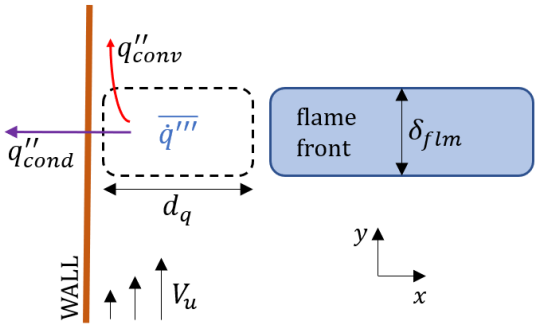

Figure 4.6: Scheme of flame quenching by conduction and convection heat losses.

In quenching, the heat lost by the flame is transferred predominately to the wall and a smaller portion

to the unburnt mixture. The energy balance can be written as:

$$\begin{aligned}
&\overline{\dot{q}'''_q}\,(d_q\,\delta_{flm}\,l) = \\
&= (\delta_{flm}\,l) \times (q'''_{cond} + q'''_{conv}) = \\
&= (\delta_{flm}\,l)\,\left[\overline{\kappa}_u \frac{T_{flm} - T_{wall}}{d_q} + h\,(T_{flm} - T_{wall})\right]
\end{aligned} \tag{4.7}$$

Introducing the Nusselt number Nu in the equation:

$$\begin{aligned}
\overline{\dot{q}'''_q}\,d_q = \overline{\kappa}_u \frac{T_{flm} - T_{wall}}{d_q}\left(1 + \frac{h\,d_q}{\overline{\kappa}_u}\right) = \\
= \overline{\kappa}_u \frac{T_{flm} - T_{wall}}{d_q}\,(1 + Nu)
\end{aligned} \tag{4.8}$$

Rearranging the terms of the equation, we obtain:

$$\overline{\dot{q}'''_q} d_q^2 = (\overline{\kappa}_u \Delta T)\,(1 + Nu) \tag{4.9}$$

Boust *et al.* [26] related the non-dimensional heat transfer to the wall, $\varphi = q_{in}/P_{flm}$, with the non-dimensional quenching distance (Peclet quenching number Pe_q), $Pe_q = d_q/\delta_{flm}$, through the equation:

$$\varphi = \frac{1}{1 + Pe_q} \tag{4.10}$$

The authors assumed that $T_{flm} - T_{wall} \approx T_{flm} - T_u$ which is valid since the flame propagates towards the unheated wall. The model was valid from HOQ to SWQ because, during the flame propagation along the wall (transient process), the temperature of the wall is, in fact, always cold and equal to the unburnt gases temperature. However, the same simplification cannot be made for our setup. In addiction, their formulation only accounts for heat losses by conduction.

For a laminar flow parallel to a flat plate, Nu can be written as a function of Re and the Prandtl numbers Pr :

$$Nu \propto Re^{1/2}\,Pr^{1/3} \tag{4.11}$$

We assumed that the small fluctuation of T_{flm} would be approximately equal to ones of T_{wall} and therefore, the difference $T_{flm} - T_{wall}$ would remain approximately constant. For the clay wall, $T_{flm} - T_{wall}$ = 1500 - 700 = 800K, and $T_{flm} - T_{wall}$ = 1500 - 400 = 1100K for the GS wall. The thermal conductivity and the Prandtl of the unburnt mixture were evaluated at the mean temperature of 1100K and 950K, for the clay and GS walls respectively, for the different fuel blends and equivalence ratios. The values of each property did not change significantly between conditions. The mean values of $\overline{\kappa}_{mix}$ and Pr are presented in Table 4.3.

Since κ_u and ΔT were considered constant for the range of fuels and flame conditions used, then, for a fixed Re, Equation 4.9 can be reduced to:

$$\overline{\dot{q}'''_q} d_q^2 = a \tag{4.12}$$

where as is constant for a given Re and wall material. Therefore, if quenching is dominated by heat losses, we get the relation $d_q \propto \overline{\dot{q}'''_q}^{-0.5}$.

Table 4.3: Average $\pm$ u_σ values of $\overline{\kappa}_u$ and Pr for all conditions tested and the temperature at which they were evaluated.

Wall	$\overline{\kappa}_u$ [W/mk]	Pr	$(T_{flm} + T_{wall})/2$ [K]
Clay	0.0845 ± 0.0015	0.6988 ± 0.0092	1100
GS	0.0751 ± 0.0017	0.6973 ± 0.0104	950

Previous authors [34, 44] have reported a linearity between the HRR and the concentration of the OH* radical , for CH_4, biogas and H_2 enriched biogas premixed flames. We used the chemiluminescence of OH* at the flame tip to estimate an average HRR in the quenching region. From the images acquired, at the same height of the pixel considered to measure the quenching distance, we extracted the intensity of the OH* radical, I_{OH}, over a horizontal line

$$\overline{\dot{q}'''_q} = c\,\overline{\dot{q}'''_{q,OH}} = c\,\frac{\int_{x_{flm,1}}^{x_{flm,2}} I_{OH} dx}{(x_{flm,2} - x_{flm,1}) \times l_s} \tag{4.13}$$

where $x_{flm,1}$ and $x_{flm,2}$ are pixel coordinates [m] of the left and right limits of the normalized 25% pixel intensity of OH* chemiluminescence, I_{OH}. Data points were fitted to curves of the type:

$$d_q = a\,\overline{\dot{q}'''_{q,OH}}^{-0.5} \tag{4.14}$$

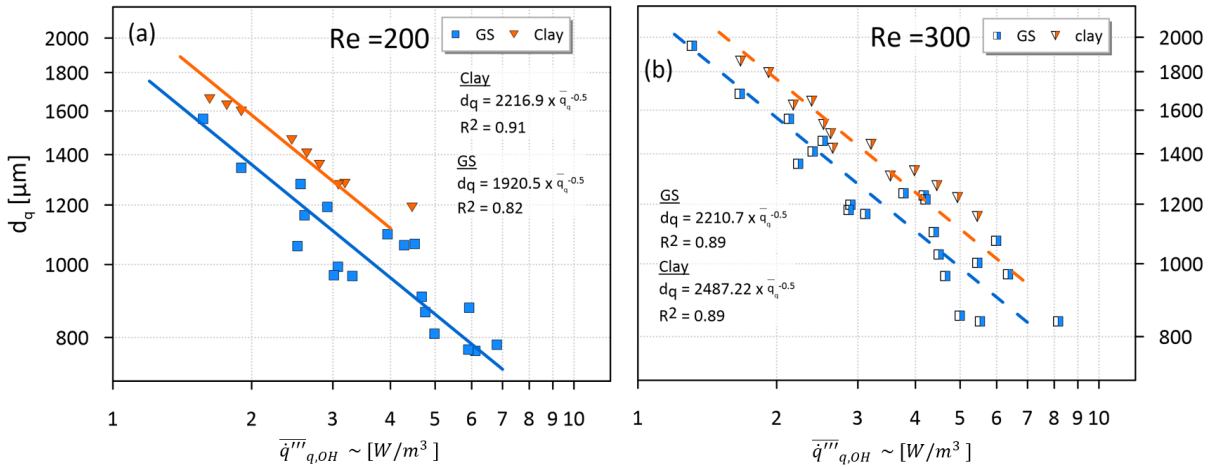

Figure 4.7: Quenching distance dependence on the average HRR in the flame tip for (a) Re = 200 and (b) Re = 300; both quantities d_q and $\overline{\dot{q}'''_{q,OH}}$ are obtained from OH* chemiluminescence.

The curves obtained from Equation 4.14 (Figure 4.7) show good correlation with the experimental values, with coefficients of determination above $R^2 > 0.8$. Deviations from the fitting curve may be due to (i) a non pure linear relation between $\overline{\dot{q}'''_q}$ and OH* chemiluminescence; (ii) the existence of radical recombination reactions.

For the same fuel and work condition, the values of $\overline{\dot{q}'''_{q,OH}}$ are approximately equal between GS and

clay, meaning that more energy is being lost when the flame interacts with the clay wall, since quenching distances are larger. On the other hand, the clay wall acts as an insulator and the heat that is transferred to the wall by conduction is less than with the GS wall. Therefore, the FWI with the clay wall must result in more heat losses by convection.

Since $\overline{\kappa_u}$, ΔT and Pr in Equation 4.9 are equal for the same fuel blend and equivalence ratios, the higher values of the parameter a for $Re = 300$ (Equation 4.14) show in Figure 4.7 suggest that the convection contribution for heat losses in quenching increases with the unburnt mixture velocity. From the parameters a obtained for clay and GS and Equation 4.9, we can write:

$$\begin{aligned} &\frac{\left[c\overline{\dot{q}'''_{q,OH}}d_q^2\right]_{clay}}{\left[c\overline{\dot{q}'''_{q,OH}}d_q^2\right]_{GS}} = \frac{[\kappa_{mix}\Delta T(1+Nu)]_{clay}}{[\kappa_{mix}\Delta T(1+Nu)]_{GS}} = \left(\frac{a_{clay}}{a_{GS}}\right)^2 \Rightarrow \\ &\Rightarrow \frac{(1+Nu)_{clay}}{(1+Nu)_{GS}} \approx \frac{0.0751 \times 1100}{0.0845 \times 800}\left(\frac{2487.2}{2210.7}\right)^2 = 1.547 \end{aligned} \tag{4.15}$$

This means that convective heat losses in the quenching region are greater with the clay wall. Furthermore, the higher surface temperatures cause a lower unburnt mixture density, compared to the FWI with the GS wall, which lead higher velocities in the quenching zone and, ultimately, to higher quenching distances. The higher porosity of the clay surface could also promote radical recombination reactions, which could force the flame to extinguish at higher distances from the wall.

4.3 Velocity field

Since large part of the total heat transferred to the wall is done by convection, the visualization of the velocity field using PIV techniques permitted a better understanding of trends observed for P_{TEG} and η_{HT}.

The divergence of velocity contours, shown in Figure 4.8a, helps to identify the flame front. The rapid increase of flow temperatures leads to a sudden change in the flow's density which by the continuity leads to a positive value of the velocity divergence:

$$\nabla\left(\rho\,\vec{V}\right) = V_x\,\frac{\partial\,\rho}{\partial x} + V_y\,\frac{\partial\,\rho}{\partial y} + \rho\,\nabla\vec{V} = 0 \tag{4.16}$$

According to numerical studies of flame wall interaction in SWQ configuration, the strongest temperature gradients occur in the flame front [38, 42, 51]. As the left jet of unburnt mixture ignites, streamlines curve away from the wall, due to the reduction in gas density and the presence of the wall. On the right branch, the thermal expansion of the gases away from the wall influences how the flame stabilizes, which combined with the absence of walls leads to a gradual consumption of the unburnt mixture, that flows almost normal to the flame speed.

The increase of the Reynolds number lead to the increase in the magnitude of velocities and the combustion products moving further away from the wall, illustrated for BG100 flames with $Re = 200$ and $Re = 300$ in Figure 4.8a and 4.8b, respectively.

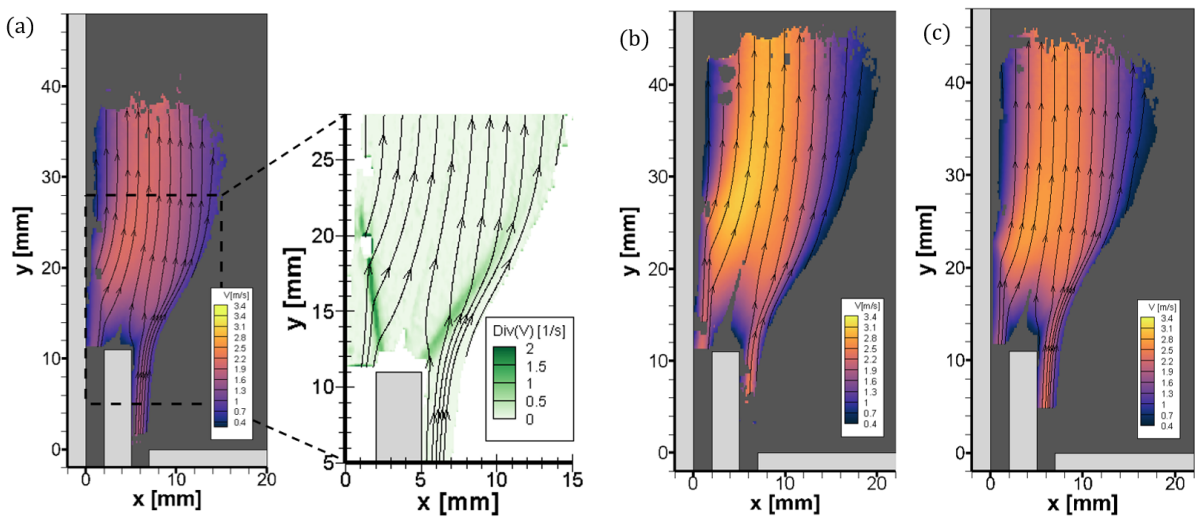

Figure 4.8: Velocity magnitudes and streamlines for BG100 flames at $\phi = 0.7$: (a) $Re = 200$ and velocity divergence $\nabla\vec{V}$; (b) $Re = 300$ with the clay wall; (c) $Re = 300$ with GS wall.

Velocity magnitudes profiles were taken at y = 35mm, where the flow is predominantly vertical, and are shown in Figure 4.9. Data points relative to the GS wall at $Re = 200$ have been omitted for the sake of clarity. For each material, two distinct groups of curves can be identified, each with its own characteristic Reynolds Number.

For flames with $Re = 300$, the peak velocity was *ca.* 0.8 m/s higher than with $Re = 200$. Increasing the equivalence ratio from $\phi = 0.7$ to $\phi = 0.8$ (BG60, $Re = 200$) led to higher velocities, *ca.* 0.1 m/s in peak velocity at y= 35 mm. However when increasing from $\phi = 0.8$ to $\phi = 0.9$, the maximum velocity remained almost constant but in a position further away from the wall. The increase of T_{wall} causes a decrease in the gases viscosity, increasing the buoyancy forces, which accelerate the fluid and lead to higher velocities on the right end of the profiles. Increasing T_{flm} is also accompanied with the increase on flame speed V_{flm} which results in a lower flame height and larger area of heat transfer. Higher temperature gradients in the vicinity of the wall ($x = 0$) result in a higher q_{conv} and η_{HT}.

The increase of Re results in higher quantities of heat released (P_{flm}) and higher gas temperatures along the y coordinate due to the stronger advection. However, it also leads to a larger portion of P_{flm} to be lost to the atmosphere (due to thermal expansion) and a reduction in the area of heat transfer, which explain the decrease of η_{HT} for a fixed ϕ seen in section 4.1.

For the same fuel and work condition, velocities magnitude were greater when using the clay wall (comparing 4.8b and 4.8c for BG100 flames at $\phi = 0.7$ and $Re = 300$ interacting with the clay and GS walls, respectively).

From the data points extracted at y = 35mm, the difference in the maximum velocity magnitude was *ca.* 0.3 m/s for $Re = 300$ (Figure 4.9). Since less heat passes through the wall and the surface is at a higher temperature than the GS surface, the lower thermal gradient may lead to lower gas densities which would lead to higher buoyancy forces, accelerating the flow and resulting in higher velocities.

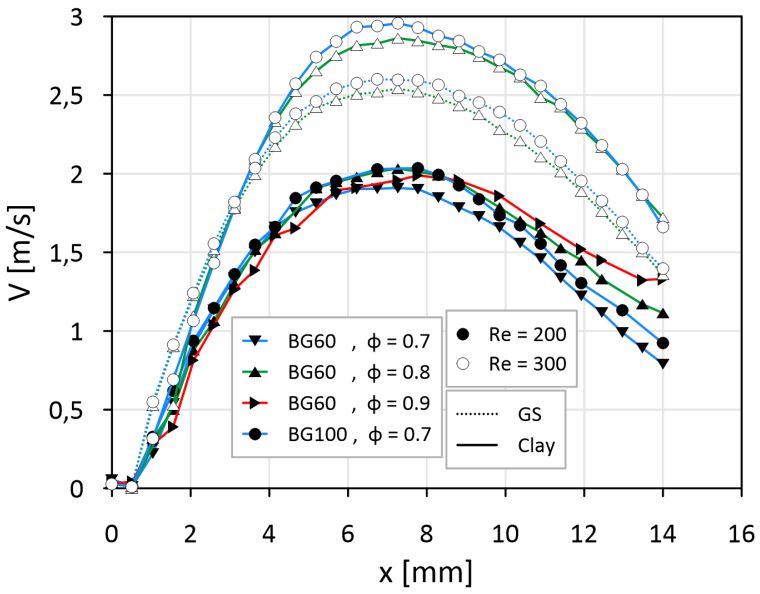

Figure 4.9: Velocity profiles at $y = 35$ mm; each fuel mixture has a distinct marker; filled markers denoted the velocities with $Re = 200$ whilst hollowed markers correspond to those with $Re = 300$; solid lines indicate the results with the clay wall while dotted lines the ones with the GS wall.

4.4 Metamaterials

In section 4.1, it was shown that it is possible to generate electricity using clay as a wall material but with lower efficiencies than other materials. In the context of the rural application of a TEG with a clay combustor, even though having electricity might be more important than the efficiency of the system, improvements are always possible. To improve the heat transfer of the clay wall, metal swarfs could be placed within the wall to form a metamaterial and create:

- A thin wall in the middle to dissipate the heat evenly across the TEG surface and reduce the thermal gradient, specially in regions closest to the flame quenching (Figure 4.10a).
- An z-shape profile that transfers the heat from the flame quenching region to a section of the TEG upstream (Figure 4.10b).

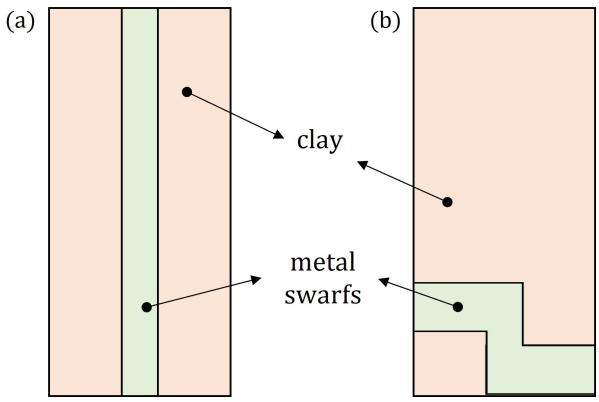

Figure 4.10: Scheme of metal swarfs arrangement; the flame interacts with the wall on the left side and TEG is place on right side of the wall.

The performance of these metamaterials was evaluated using the mathematical model. As reference thermal conductivity of a metal swarfs, it was used $k_{wall} = 56.7$ [W/mK] of GS. For the case illustrated in Figure 4.10a termed henceforth sandwich, it was considered an interior wall with thickness $t = 1$mm and a total thickness of $t_{wall} = 7.5$mm, so that the wall thermal resistance remained approximately equal to the clay wall used in this work ($t_{wall} = 6.5$ mm). In the case of the z-shape profile, the thickness of the horizontal and vertical sections was 5 mm and 3 mm, respectively, and $t_{wall} = 7.5$ mm.

The flame condition chosen to evaluate the metamaterials was the one that yielded the highest temperatures at the TEG hot side, with the clay wall, *i.e.* BG80, $\phi = 1$ and $Re = 350$. For that condition, P_{TEG} was 3.40 W, obtained with the model.

The P_{TEG} obtained with the sandwich and z-shape metamaterials was 3.49 W and 3.55 W, respectively, which corresponds to an increase of 2.6% and 4.4%. Figures 4.11a and b illustrate the temperature distributions and the heat flux streamlines of the sandwich and z-shape metamaterials, respectively.

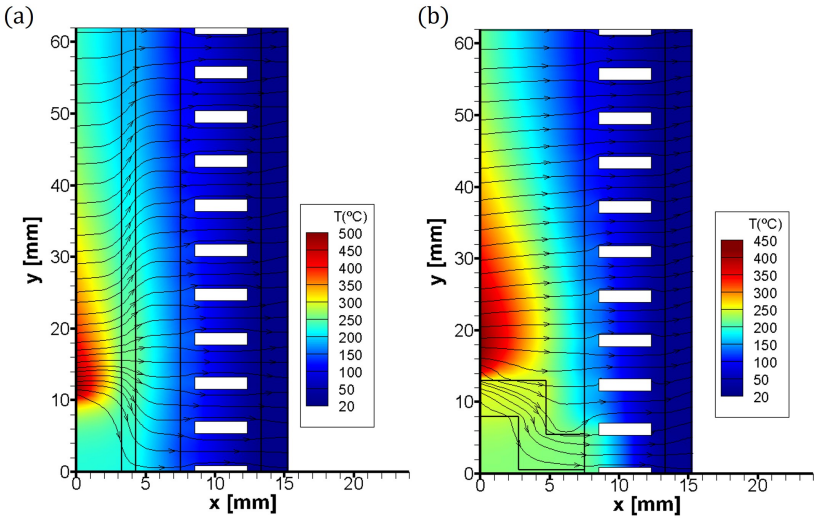

Figure 4.11: Temperature distribution and streamlines of (a) sandwich and (b) z-shape metamaterials.

In the case of the sandwich metamaterial, one can see that heat streamlines curve as they approach the metallic section (3.5 mm $< x <$ 4.5 mm, Figure 4.12a), leading to a more uniform temperature distribution along the hot surface (Figure 4.12a), compared to the clay wall. Regarding, the wall with the z-shape profile, heat is conducted to the bottom of the TEG causing an increase of surface temperatures beyond $T_{H,max} = 200\,$°C (Figure 4.12b).

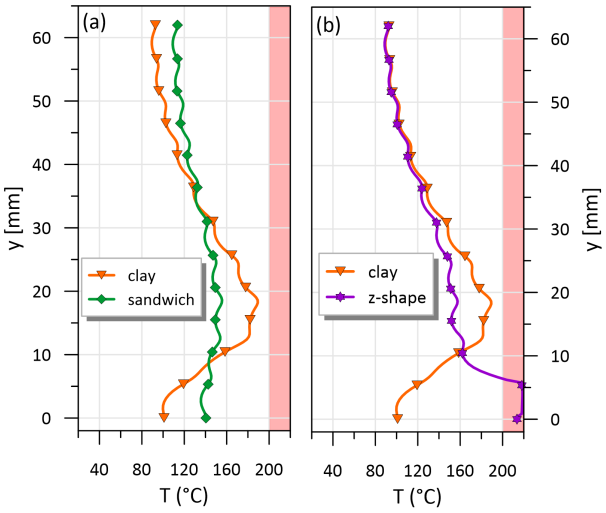

Figure 4.12: Temperature distribution at the TEG hot side (x=7.5 mm) with the clay and (a) sandwich and (b) z-shape metamaterials walls.

Chapter 5

Conclusions

5.1 Overview of work performed

The main objective of this work was to evaluate the potential use of clay as a wall material in the direct heat-to-electricity power conversion using a thermoelectric generator. The influence of wall material to the system performance (TEG output power and efficiency) and to the flame wall interaction (d_q, heat release rate and velocity field) was studied. A mathematical model was developed, based on the finite element method, to complement the analysis of the contribution of the wall (thermal conductivity and thickness) to the electrical power generated.

Walls made of clay and GS were tested. The results with the GS wall were used as reference, to compare with the clay wall. Each wall was studied with seven fuel blends. BG100 and two biogas mixtures (BG80 and BG60), to which H_2 was added in small quantities (up to 20%), were selected. Each fuel blends was studied with a range of equivalence ratios (from 0.7 to 1.0) and burner Reynolds number (from 100 to 350). Chemiluminescence of OH* and CH* radicals was used to evaluate the influence of wall material in the heat release rate and quenching distances. Velocity fields were investigated using PIV techniques.

5.2 Achievements

The main findings of the present work are:

1. P_{TEG} and η_{TEG} increase significantly with ϕ, regardless of the wall material. Changes in Re cause variations of P_{TEG} with the GS wall, but not with the clay one. The increase of Re causes large drops in η_{glob}. The difference in P_{TEG} between wall materials increases with flame temperature.

2. For a flame in SWQ, d_q are larger with the clay wall than with the GS wall. The chemiluminescence intensity of the radical OH* was related with $d_q^{-0.5}$ (with a coefficient of determination $R^2 > 0.8$). The increase of unburnt mixture velocity causes higher convective heat losses. The convection contribution for heat losses in the quenching zone is greater when the clay wall is used.

3. The decrease in gases density in the flame front causes streamlines to deviate away from the wall right after the quenching region. Higher temperatures at the clay surface decreases gases density in the vicinity of the wall, resulting in higher velocities.

4. The mathematical model developed showed an excellent agreement with the experimental results, with an average error under 7%.

5.3 Future Work

The results obtained with the mathematical model, regarding the use of metamaterials to design the wall might serve as starting point for its experimental investigation. Other designs of metamaterials could also be studied using the model developed.

In the perspective of the application of the TEG as an electricity source, different heat exchanger setup should be considered, such as:

1. A closed water circuit using a small pump powered by the TEG. This could maintain the temperature gradient across the TEG legs, and therefore its efficiency, relative to the experimental setup used in this work.

2. Replace the heat exchanger by a finned heat sink assembled to a water reservoir. Opposite to the previous idea, this setup would not need a water pump, hence the power yield would be higher during short periods. Over time, the increase in water temperature would lead to a decrease in $T_H - T_C$ and electrical power output.

3. A similar concept to the one presented in the first topic would be to use a finned heat exchanger assembled to a fan powered by the TEG, to increase convection over the fins. That system would not require water and would generate a constant power output. However, the likely lower convective coefficient (due to the relative specific heat of air, when compared to water) could lead to higher temperatures on the cold side of the TEG and, subsequentially, lower power yielded.

Bibliography

[1] United Nations. The Paris Agreement. URL `https://unfccc.int/process-and-meetings/the-paris-agreement/the-paris-agreement`.

[2] Our World in Data. Acess to electricity. URL `https://ourworldindata.org/energy-access#access-to-electricity`.

[3] *Thermoelectrics Handbook*. CRC Press, 2006. doi: 10.1201/9781420038903.

[4] A. Vaccari. Clays and catalysis: a promising future. *Applied Clay Science*, 14(4):161–198, 1999. ISSN 0169-1317. doi: https://doi.org/10.1016/S0169-1317(98)00058-1.

[5] M. Hamid Elsheikh, D. A. Shnawah, M. F. M. Sabri, S. B. M. Said, M. Haji Hassan, M. B. Ali Bashir, and M. Mohamad. A review on thermoelectric renewable energy: Principle parameters that affect their performance. *Renewable and Sustainable Energy Reviews*, 30:337–355, 2014. ISSN 1364-0321. doi: https://doi.org/10.1016/j.rser.2013.10.027.

[6] M. K. K. Govardhan Neeli, Dilip Kumar Behara. State of the art review on thermoelectric materials. *International Journal of Science and Research*, 5:1833 – 1844, 10 2016. doi: 10.21275/ART20162476.

[7] G. Min and D. M. Rowe. Conversion efficiency of thermoelectric combustion systems. *Energy Conversion, IEEE Transactions on*, 22:528 – 534, 07 2007. doi: 10.1109/TEC.2006.877375.

[8] A. Narjis, C.-T. Liang, H. E. Aakib, A. Tchenka, and A. Outzourhit. Design optimization for maximized thermoelectric generator performance. *Journal of Electronic Materials*, 49:306–310, 2019. doi: 10.1007/s11664-019-07748-9.

[9] S. B. Riffat and X. Ma. Thermoelectrics: a review of present and potential applications. *Applied Thermal Engineering*, 23(8):913–935, 2003. ISSN 1359-4311. doi: https://doi.org/10.1016/S1359-4311(03)00012-7.

[10] T. Kuroki, R. Murai, K. Makino, K. Nagano, T. Kajihara, H. Kaibe, H. Hachiuma, and H. Matsuno. Research and development for thermoelectric generation technology using waste heat from steelmaking process. *Journal of Electronic Materials*, 44(6):2151–2156, Mar 2015. doi: 10.1007/s11664-015-3722-8.

[11] J. H. Panya Yodovard, Joseph Khedari. The potential of waste heat thermoelectric power generation from diesel cycle and gas turbine cogeneration plants. *Energy Sources*, 23(3):213–224, 2001. doi: 10.1080/00908310151133889.

[12] R. Vullers, R. van Schaijk, I. Doms, C. Van Hoof, and R. Mertens. Micropower energy harvesting. *Solid-State Electronics*, 53(7):684–693, 2009. ISSN 0038-1101. doi: https://doi.org/10.1016/j.sse.2008.12.011. Papers Selected from the 38th European Solid-State Device Research Conference – ESSDERC'08.

[13] K. F. Mustafa, S. Abdullah, M. Z. Abdullah, and K. Sopian. A review of combustion-driven thermoelectric (te) and thermophotovoltaic (tpv) power systems. *Renewable and Sustainable Energy Reviews*, 71:572–584, 2017. ISSN 1364-0321. doi: https://doi.org/10.1016/j.rser.2016.12.085.

[14] K. Hiranandani, B. Aravind, V. Ratna Kishore, and S. Kumar. Development of a numerical model for performance prediction of an integrated microcombustor-thermoelectric power generator. *Energy*, 192:116624, 2020. ISSN 0360-5442. doi: https://doi.org/10.1016/j.energy.2019.116624.

[15] B. Aravind, B. Khandelwal, and S. Kumar. Experimental investigations on a new high intensity dual microcombustor based thermoelectric micropower generator. *Applied Energy*, 228:1173–1181, 2018. ISSN 0306-2619. doi: https://doi.org/10.1016/j.apenergy.2018.07.022.

[16] Review of thermoelectric geometry and structure optimization for performance enhancement. *Applied Energy*, 268:115075, 2020. ISSN 0306-2619. doi: https://doi.org/10.1016/j.apenergy.2020.115075.

[17] U. Erturun, K. Erermis, and K. Mossi. Effect of various leg geometries on thermo-mechanical and power generation performance of thermoelectric devices. *Applied Thermal Engineering*, 73(1):128–141, 2014. ISSN 1359-4311. doi: https://doi.org/10.1016/j.applthermaleng.2014.07.027.

[18] Z. L. Wei, C. W. Leung, C. S. Cheung, and Z. H. Huang. Effects of equivalence ratio, h2 and co2 addition on the heat release characteristics of premixed laminar biogas-hydrogen flame. *International Journal of Hydrogen Energy*, 41(15):6567–6580, 2016. ISSN 0360-3199. doi: https://doi.org/10.1016/j.ijhydene.2016.01.170.

[19] Z. L. Wei, C. W. Leung, C. S. Cheung, and Z. H. Huang. Effects of h2 and co2 addition on the heat transfer characteristics of laminar premixed biogas–hydrogen bunsen flame. *International Journal of Heat and Mass Transfer*, 98:359–366, 2016. ISSN 0017-9310. doi: https://doi.org/10.1016/j.ijheatmasstransfer.2016.02.064.

[20] Z. Wei, Z. He, H. Zhen, X. Zhang, Z. Chen, and Z. Huang. Kinetic modeling investigation on the coupling effects of h2 and co2 addition on the laminar flame speed of hydrogen enriched biogas mixture. *International Journal of Hydrogen Energy*, 45(51):27891–27903, 2020. ISSN 0360-3199. doi: https://doi.org/10.1016/j.ijhydene.2020.07.119.

[21] Z. Hu and X. Zhang. Experimental study on flame stability of biogas / hydrogen combustion. *International Journal of Hydrogen Energy*, 44(11):5607–5614, 2019. ISSN 0360-3199. doi: https://doi.org/10.1016/j.ijhydene.2018.08.011.

[22] H. Kosaka, F. Zentgraf, A. Scholtissek, L. Bischoff, T. Häber, R. Suntz, B. Albert, C. Hasse, and A. Dreizler. Wall heat fluxes and co formation/oxidation during laminar and turbulent side-wall quenching of methane and dme flames. *International Journal of Heat and Fluid Flow*, 70:181–192, 2018. ISSN 0142-727X. doi: https://doi.org/10.1016/j.ijheatfluidflow.2018.01.009.

[23] T. Häber and R. Suntz. Effect of different wall materials and thermal-barrier coatings on the flame-wall interaction of laminar premixed methane and propane flames. *International Journal of Heat and Fluid Flow*, 69:95–105, 2018. doi: https://doi.org/10.1016/j.ijheatfluidflow.2017.12.004.

[24] H. Yang, Y. Feng, Y. Wu, X. Wang, L. Jiang, D. Zhao, and H. Yamashita. A surface analysis-based investigation of the effect of wall materials on flame quenching. *Combustion Science and Technology*, 183(5):444–458, 2011. doi: 10.1080/00102202.2010.530323.

[25] H. Yang, Y. Feng, X. Wang, L. Jiang, D. Zhao, N. Hayashi, and H. Yamashita. Oh-plif investigation of wall effects on the flame quenching in a slit burner. *Proceedings of the Combustion Institute*, 34 (2):3379–3386, 2013. ISSN 1540-7489. doi: https://doi.org/10.1016/j.proci.2012.07.038.

[26] B. Boust, J. Sotton, S. Labuda, and M. Bellenoue. A thermal formulation for single-wall quenching of transient laminar flames. *Combustion and Flame*, 149(3):286–294, 2007. ISSN 0010-2180. doi: https://doi.org/10.1016/j.combustflame.2006.12.019.

[27] O. Ezekoye, R. Greif, and R. F. Sawyer. Increased surface temperature effects on wall heat transfer during unsteady flame quenching. *Symposium (International) on Combustion*, 24(1):1465–1472, 1992. ISSN 0082-0784. doi: https://doi.org/10.1016/S0082-0784(06)80171-2.

[28] K. T. Kim, D. H. Lee, and S. Kwon. Effects of thermal and chemical surface–flame interaction on flame quenching. *Combustion and Flame*, 146(1):19–28, 2006. ISSN 0010-2180. doi: https://doi.org/10.1016/j.combustflame.2006.04.012.

[29] T. J. Poinsot, D. C. Haworth, and G. Bruneaux. Direct simulation and modeling of flame-wall interaction for premixed turbulent combustion. *Combustion and Flame*, 95(1):118–132, 1993. ISSN 0010-2180. doi: https://doi.org/10.1016/0010-2180(93)90056-9.

[30] F. P. Incropera and D. P. DeWitt. *Fundamentals of Heat and Mass Transfer*. John Wiley & Sons, Inc., 7th edition edition, 2011.

[31] Dantec Dynamics. *DynamicStudio User's Guide*. Skovlunde, 2016.

[32] H. K. M. David G. Goodwin, Raymond L. Speth and B. W. Weber.

[33] G. P. Smith, D. M. Golden, M. Frenklach, N. W. Moriarty, B. Eiteneer, M. Goldenberg, C. T. Bowman, R. K. Hanson, S. Song, J. William C. Gardiner, V. V. Lissianski, and Z. Qin. URL `http://www.me.berkeley.edu/gri_mech/`.

[34] M. D. Santos, S. I. Dias, A. P. Gonçalves, and E. C. Fernandes. Thermoelectric power generation from biogas+h2 flames: Influence of flame-wall interaction. *Experimental Thermal and Fluid Science*, 126:110350, 2021. doi: https://doi.org/10.1016/j.expthermflusci.2021.110350.

[35] H. Kosaka, F. Zentgraf, A. Scholtissek, C. Hasse, and A. Dreizler. Effect of flame-wall interaction on local heat release of methane and dme combustion in a side-wall quenching geometry. *Flow, Turbulence and Combustion*, 104(4):1029–1046, 2019. doi: 10.1007/s10494-019-00090-4.

[36] M. Mann, C. Jainski, M. Euler, B. Böhm, and A. Dreizler. Transient flame–wall interactions: Experimental analysis using spectroscopic temperature and co concentration measurements. *Combustion and Flame*, 161(9):2371–2386, 2014. ISSN 0010-2180. doi: https://doi.org/10.1016/j.combustflame.2014.02.008.

[37] C. K. Westbrook, A. A. Adamczyk, and G. A. Lavoie. A numerical study of laminar flame wall quenching. *Combustion and Flame*, 40:81–99, 1981. ISSN 0010-2180. doi: https://doi.org/10.1016/0010-2180(81)90112-7.

[38] A. Gruber, R. Sankaran, E. R. Hawkes, and J. H. Chen. Turbulent flame-wall interaction: a direct numerical simulation study. *Journal of Fluid Mechanics*, 658:5–32, 2010. doi: 10.1017/S0022112010001278.

[39] C. Jainski, M. Rißmann, B. Böhm, J. Janicka, and A. Dreizler. Sidewall quenching of atmospheric laminar premixed flames studied by laser-based diagnostics. *Combustion and Flame*, 183:271–282, 2017. ISSN 0010-2180. doi: https://doi.org/10.1016/j.combustflame.2017.05.020.

[40] C. Jainski, M. Rißmann, S. Jakirlic, B. Böhm, and A. Dreizler. Quenching of premixed flames at cold walls: Effects on the local flow field. *Flow, Turbulence and Combustion*, 100(1):177–196, 2017. doi: 10.1007/s10494-017-9836-8.

[41] F. Quintino, T. Trindade, and E. Fernandes. Biogas combustion: Chemiluminescence fingerprint. *Fuel*, 231:328–340, 2018. ISSN 0016-2361. doi: https://doi.org/10.1016/j.fuel.2018.05.086.

[42] T. Zirwes, T. Häber, F. Zhang, H. Kosaka, A. Dreizler, M. Steinhausen, C. Hasse, A. Stagni, D. Trimis, R. Suntz, and et al. Numerical study of quenching distances for side-wall quenching using detailed diffusion and chemistry. *Flow, Turbulence and Combustion*, 106(2):649–679, 2020. doi: 10.1007/s10494-020-00215-0.

[43] M. Bellenoue, T. Kageyama, S. A. Labuda, and J. Sotton. Direct measurement of laminar flame quenching distance in a closed vessel. *Experimental Thermal and Fluid Science*, 27(3):323–331, 2003. ISSN 0894-1777. doi: https://doi.org/10.1016/S0894-1777(02)00304-7.

[44] C. Panoutsos, Y. Hardalupas, and A. Taylor. Numerical evaluation of equivalence ratio measurement using oh* and ch* chemiluminescence in premixed and non-premixed methane–air flames. *Combustion and Flame*, 156(2):273–291, 2009. ISSN 0010-2180. doi: https://doi.org/10.1016/j.combustflame.2008.11.008.

[45] R. B. Abernethy, R. P. Benedict, and R. B. Dowdell. Asme measurement uncertainty. *Journal of Fluids Engineering*, 107(2):161–164, Jun 1985. doi: 10.1115/1.3242450.

[46] J. J. Charonko and P. P. Vlachos. Estimation of uncertainty bounds for individual particle image velocimetry measurements from cross-correlation peak ratio. *Measurement Science and Technology*, 24(6), 2013. doi: 10.1088/0957-0233/24/6/065301.

[47] D. J. N. Reddy. *n Introduction to the Finite Element Method*. McGraw-Hill Education, 3rd edition edition, 2005.

[48] S. R. Turns. *An introduction to combustion: Concepts and applications*.

[49] P. Popp and M. Baum. Analysis of wall heat fluxes, reaction mechanisms, and unburnt hydrocarbons during the head-on quenching of a laminar methane flame. *Combustion and Flame*, 108(3):327–348, 1997. ISSN 0010-2180. doi: https://doi.org/10.1016/S0010-2180(96)00144-7.

[50] F. A. Williams. *Combustion Theory*. CRC Press, 1985. doi: https://doi.org/10.1201/9780429494055.

[51] S. Ganter, C. Straßacker, G. Kuenne, T. Meier, A. Heinrich, U. Maas, and J. Janicka. Laminar near-wall combustion: Analysis of tabulated chemistry simulations by means of detailed kinetics. *International Journal of Heat and Fluid Flow*, 70:259–270, 2018. ISSN 0142-727X. doi: https://doi.org/10.1016/j.ijheatfluidflow.2018.02.015.

Appendix A

Technical Datasheets

A.1 TEG GM200-49-45-30 Datasheet

GM200-49-45-30
Thermoelectric generator module

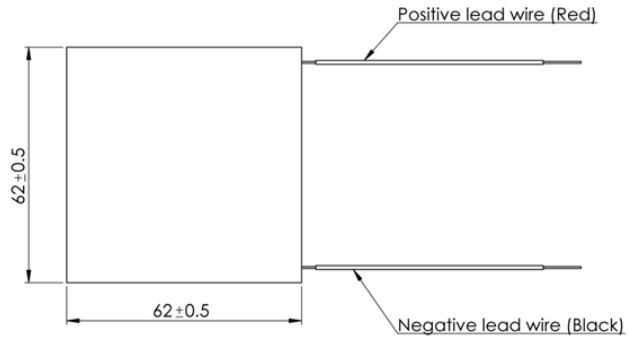

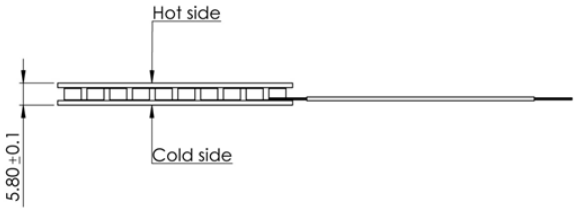

Parameters for hot side temp 200ºC and cold side temp 30ºC

Matched load output power	7.5W
Matched load resistance	0.27Ω ± 15%
Open circuit voltage	2.8V
Matched load output	5.3A
Matched load output voltage	1.4V
Heat flow through module	~149W
Maximum compress (non-destructive)	1MPa
Maximum operation temperature	Hot side - 200ºC. Cold side - 175ºC

Features

- Compact structure (no moving parts)
- Reliable performance
- Maintenance-free
- Noise-free operation
- Low-carbon, green technology

Adaptive® Power Management

Web: www.etdyn.com Tel: +44(0)116 279 6899 E-mail: info@etdyn.com

GM200-49-45-30
Thermoelectric generator module

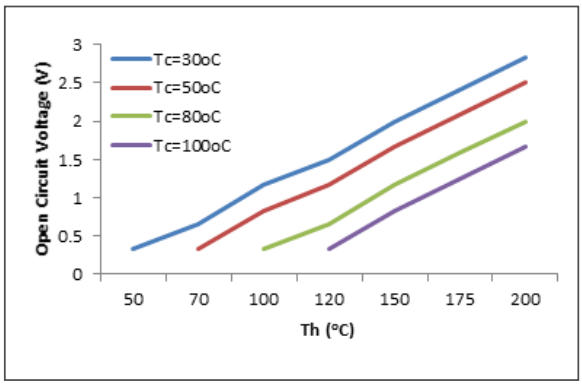

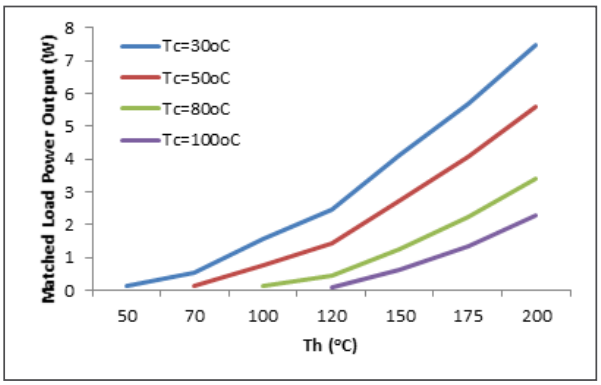

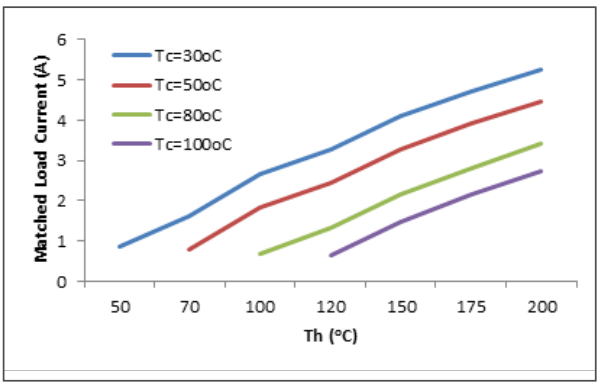

Note: Th = hot side temperature

Adaptive® Power Management

Adaptive is a registered trademark of European Thermodynamics Limited.
Web: www.etdyn.com Tel: +44(0)116 279 6899 E-mail: info@etdyn.com

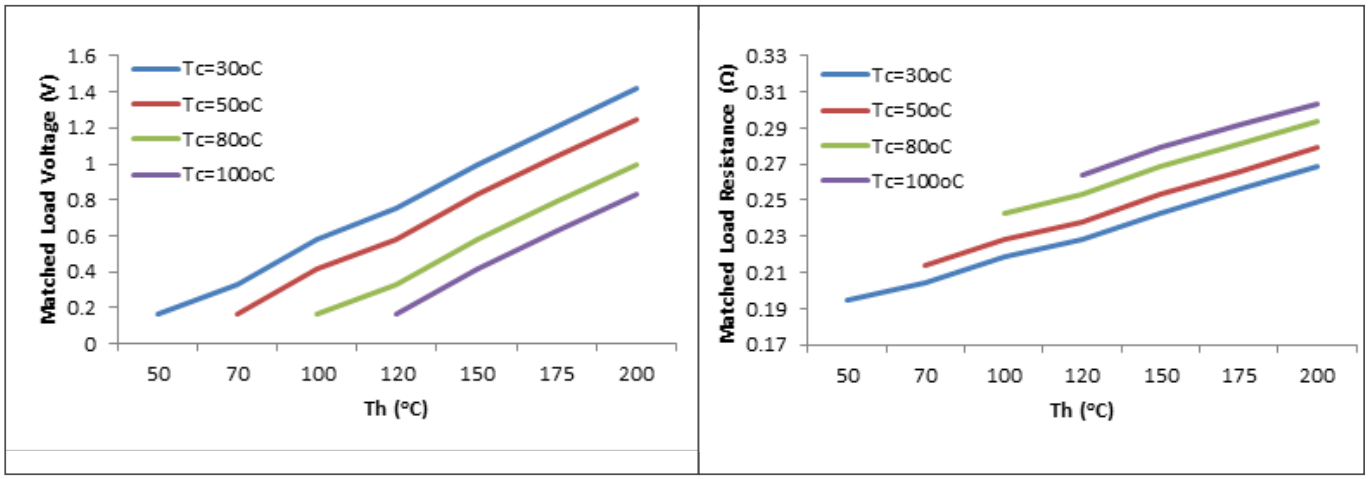

Note: Th = hot side temperature

GM200-49-45-30
Thermoelectric generator module

Formulae for calculating thermoelectric properties (best fit derived from measured material characteristics)

Thermal conductivity

- $k_n = (0.0000334545 \times T^2 - 0.023350303 \times T + 5.606333)$ W/mK
- $k_p = (0.000036155 8 \times T^2 - 0.026351342 \times T + 6.22162)$ W/mK

Seebeck coefficient

- $a_n = (0.001530736 \times T^2 - 1.08058874 \times T - 28.338095) \times 10^{-6}$ V/K
- $a_p = (-0.003638095 \times T^2 + 2.74380952 \times T - 296.214286) \times 10^{-6}$ V/K

Electrical conductivity

- $o_p = (0.015601732 \times T^2 - 15.708052 \times T + 4466.38095) \times 10^2$ S/m
- $o_n = (0.01057143 \times T^2 - 10.16048 \times T + 3113.71429) \times 10^2$ S/m

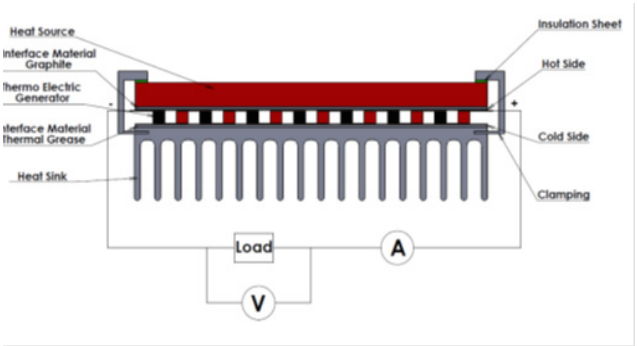

Where the subscript *n* refers to the n-type thermoelement and the subscript *p* refers to the p-type thermoelement.It should be noted here that the electrical conductivity relates to the electrical resistivity as follows: p= 1/o Thus, where electrical resistivity is needed, one can calculate the electrical conductivity through the aforementioned formulae and then reverse to calculate the electrical resistivity.

Adaptive® Power Management

Adaptive is a registered trademark of European Thermodynamics Limited.
Web: www.etdyn.com Tel: +44(0)116 279 6899 E-mail: info@etdyn.com

Appendix B

Results annexes

B.1 Power and efficiency mapas

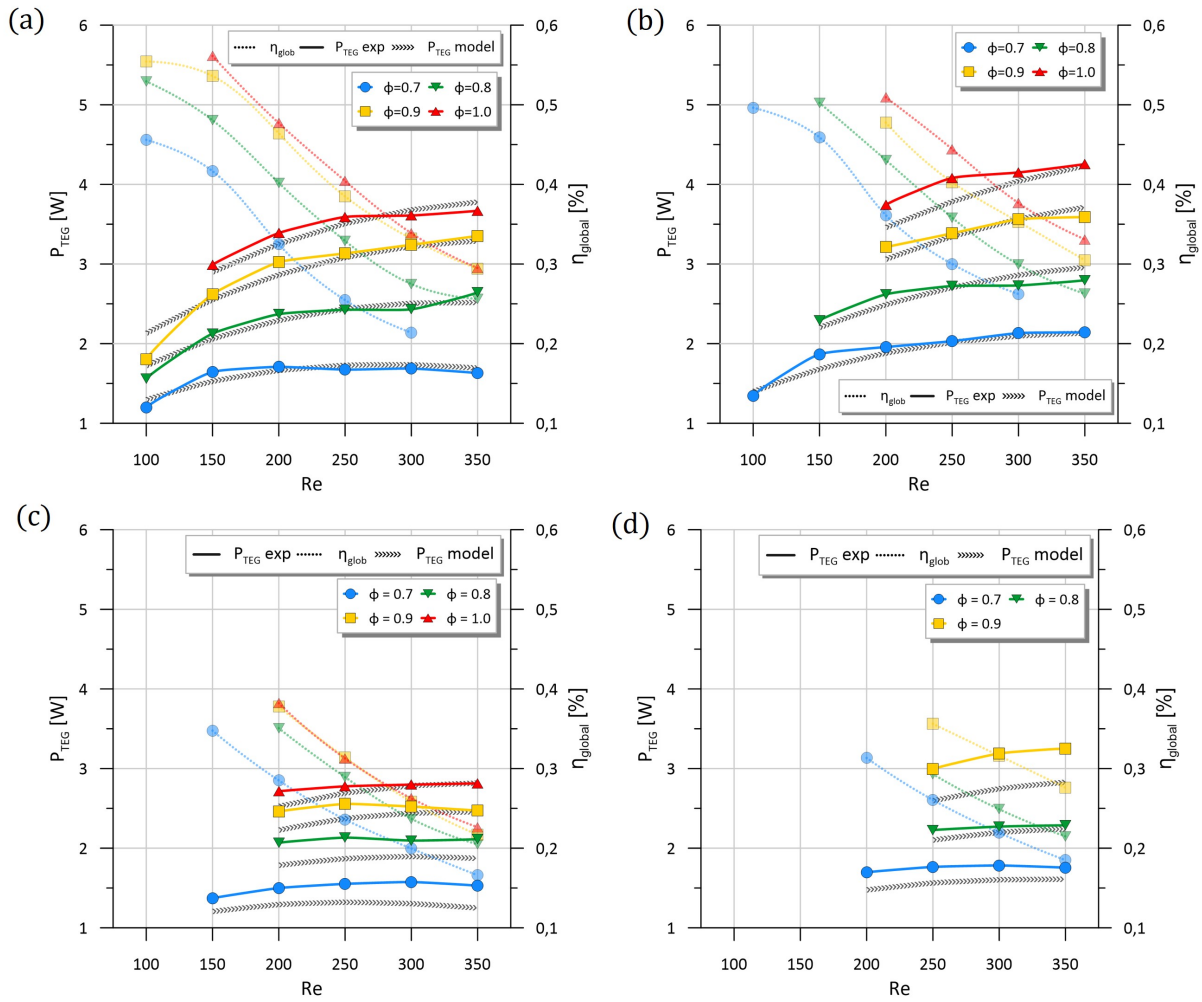

Figure B.1: Maps of P_{TEG} and η_{glob} for (a) BG60 and (b) BG60 + 20% H_2 for with the GS wall, and (c) BG60 and (d) BG60 + 20% H_2; continuous lines link experimental P_{TEG} whilst dotted lines correspond to η_{glob}; black lines denote the values obtained with the mathematical model

Appendix C

Wall analysis

C.1 Clay microscopic image

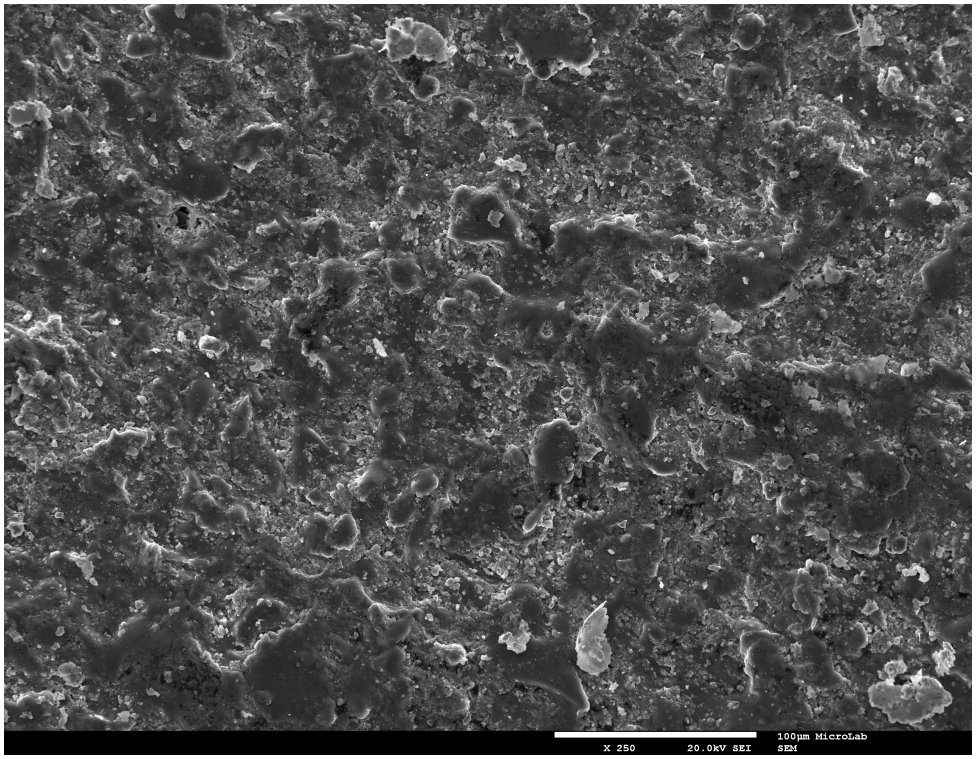

Figure C.1: Microscopic image of the clay wall using Scanning Electron Microscopy (SEM).

C.2 Chemical surface analysis

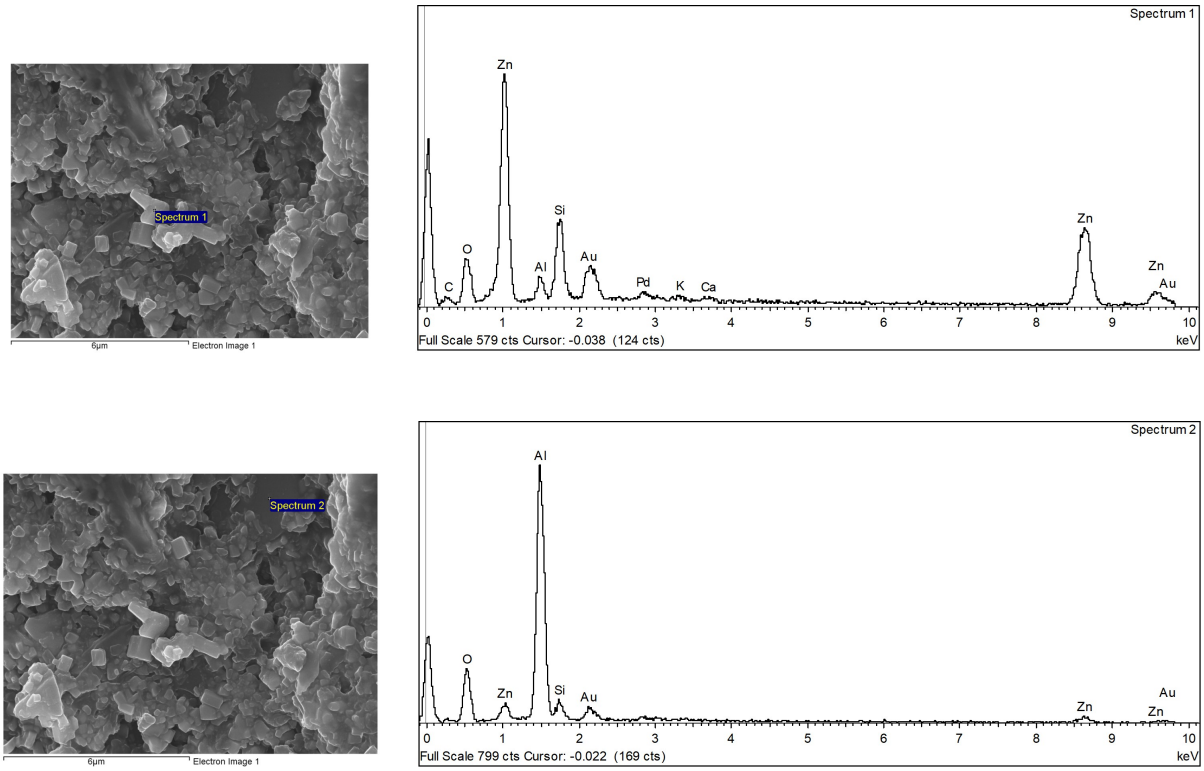

Figure C.2: Energy dispersive X-ray spectroscopy (EDS) spectrum of the clay surface, perform on two crystals.

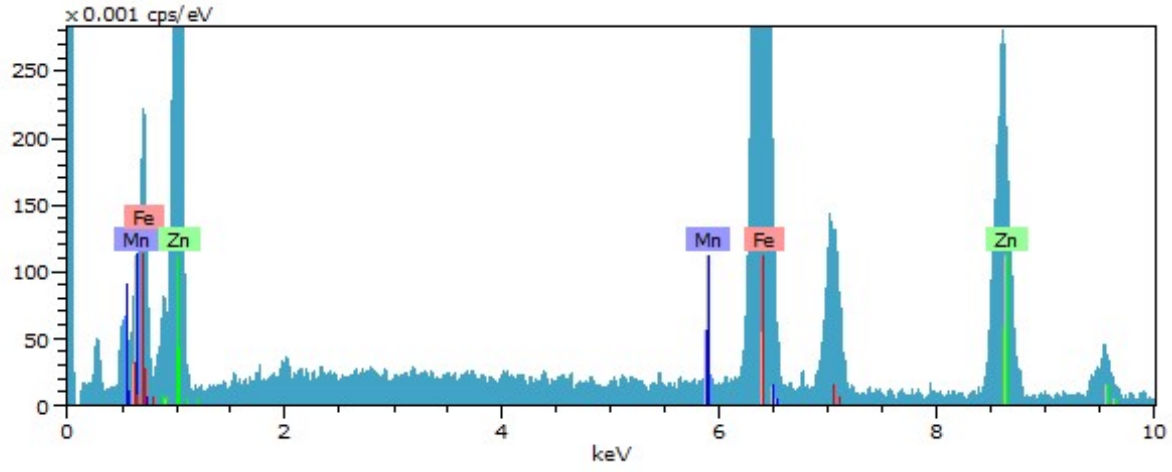

Figure C.3: EDS spectrum of the galvanized steel surface.